



University of Tennessee, Knoxville
**TRACE: Tennessee Research and Creative
Exchange**

Doctoral Dissertations

Graduate School

12-2008

Modeling of AlGa_N/Ga_N High Electron Mobility Transistor for Sensors and High-Temperature Circuit Applications

Sazia Afreen Eliza

University of Tennessee - Knoxville

Follow this and additional works at: https://trace.tennessee.edu/utk_graddiss

 Part of the [Electrical and Computer Engineering Commons](#)

Recommended Citation

Eliza, Sazia Afreen, "Modeling of AlGa_N/Ga_N High Electron Mobility Transistor for Sensors and High-Temperature Circuit Applications. " PhD diss., University of Tennessee, 2008.
https://trace.tennessee.edu/utk_graddiss/514

This Dissertation is brought to you for free and open access by the Graduate School at TRACE: Tennessee Research and Creative Exchange. It has been accepted for inclusion in Doctoral Dissertations by an authorized administrator of TRACE: Tennessee Research and Creative Exchange. For more information, please contact trace@utk.edu.

To the Graduate Council:

I am submitting herewith a dissertation written by Sazia Afreen Eliza entitled "Modeling of AlGa_N/Ga_N High Electron Mobility Transistor for Sensors and High-Temperature Circuit Applications." I have examined the final electronic copy of this dissertation for form and content and recommend that it be accepted in partial fulfillment of the requirements for the degree of Doctor of Philosophy, with a major in Electrical Engineering.

Syed K. Islam, Major Professor

We have read this dissertation and recommend its acceptance:

Benjamin J. Blalock, Leon M. Tolbert, Mohamed R. Mahfouz

Accepted for the Council:

Carolyn R. Hodges

Vice Provost and Dean of the Graduate School

(Original signatures are on file with official student records.)

To the Graduate Council:

I am submitting herewith a dissertation written by Sazia Afreen Eliza entitled “Modeling of AlGa_N/Ga_N High Electron Mobility Transistor for Sensors and High-Temperature Circuit Applications.” I have examined the final electronic copy of this dissertation for form and content and recommend that it be accepted in partial fulfillment of the requirements for the degree of Doctor of Philosophy, with a major in Electrical Engineering.

Dr. Syed K. Islam

Major Professor

We have read this dissertation and recommend its acceptance:

Dr. Benjamin J. Blalock

Dr. Leon M. Tolbert

Dr. Mohamed R. Mahfouz

Accepted for the Council:

Carolyn R. Hodges

Vice Provost and Dean of the Graduate School

(Original signatures are on file with official student records.)

Modeling of AlGaN/GaN High Electron Mobility Transistor for Sensors and High-Temperature Circuit Applications

A Dissertation
Presented for the
Doctor of Philosophy Degree

The University of Tennessee, Knoxville

Sazia Afreen Eliza
December 2008

Dedication

This dissertation is dedicated to my parents, my sister and my husband.

Acknowledgements

I am ever grateful to some persons for the completion of this dissertation work. First of all, I like to name my major advisor Dr. Syed K. Islam. Without his continuous encouragement and directions, this work would have been impossible. I am grateful to Dr. Benjamin J. Blalock, Dr. Leon M. Tolbert and Dr. Mohamed R. Mahfouz beside my major advisor for being the members of my dissertation committee and providing important feedback on my work. I am also grateful to Dr. Syed K. Islam and Dr. Mohamed R. Mahfouz for the financial support throughout my Ph.D. program.

I am thankful to Dr. Ida Lee for giving the opportunity to work with her in Molecular Bioscience and Biotechnology group at Oak Ridge National Laboratory. I am grateful to her for providing me a test result and also for her direct help and the indirect help with part of my dissertation work. In this regard, I also like to express my gratitude to Mr. Miguel Rodriguez Jr., Dr. Barbara Evans, Dr. Elias Greenbaum and Dr. M. Nance Ericson. I am grateful to Mohammad Aminul Huque, Touhidur Rahman and Mohammad Rafiqul Haider as my co-researchers in various projects and all other members of Analog, VLSI and Devices Laboratory for their friendly support during my Ph.D. program. I am grateful to Dr. Asif Khan from University of South Carolina for providing me the devices and Dr. Yanqing Deng for having fruitful discussion about the device parameters.

Abstract

With the most advanced and mature technology for electronic devices, silicon (Si) based devices can be processed with practically no material defects. However, Si technology has difficulty meeting the demand for some high-power, high-speed, and high-temperature applications due to limitations in its intrinsic properties. Wide bandgap semiconductors have greater prospects compared to Si based devices. The wide band gap material system shows higher breakdown voltage, lower leakage, higher saturation velocity, larger thermal conductivity and better thermal stability suitable for high-power, high-speed, and high-temperature operations of the devices. In recent years, GaN based devices have drawn much research attention due to their superior performances compared to other wide bandgap semiconductor (SiC) devices. Specifically, implementation of AlGaIn/GaN high electron mobility transistor (HEMT) based power amplifiers have become very promising for applications in base stations or radar. With the increase in device power, channel temperature rises. This introduces high-temperature effects in the device characteristics. In addition, high-power, high-frequency and high-temperature operation of AlGaIn/GaN HEMT is required for telemetry in extreme environment.

AlGaIn/GaN HEMT also shows great potential as chemically selective field-effect transistor (CHEMFET). Due to simpler imprint technique and amplification advantages CHEMFET based detection and characterization of bio-molecules has become very popular. AlGaIn/GaN HEMT has high mobility two-dimensional electron gas (2 DEG) at the hetero-interface closer to the surface and hence it shows high sensitivity to any surface charge conditions.

The primary objective of this research is to develop a temperature dependent physics based model of AlGaIn/GaN HEMT to predict the performance for high-power and high-speed applications at varying temperatures. The physics based model has also been applied to predict the characteristics of AlGaIn/GaN HEMT based CHEMFET for the characterization of bio-molecular solar batteries - Photosystem I reaction centers. Using the CHEMFET model, the number of reaction centers with effective orientation on the gate surface of the HEMT can be estimated.

Table of Contents

Chapter 1	Introduction.....	1
1.1	Introduction.....	1
1.2	Motivation of Research.....	1
1.2.1	Wide Bandgap Semiconductors.....	2
1.3	Introduction to HEMT.....	5
1.4	GaN HEMT Technology.....	7
1.4.1	Prospects of GaN HEMT.....	10
1.4.2	Potential of AlGaIn/GaN HEMT as CHEMFET.....	14
1.5	Research Objectives.....	15
1.6	Outline of Dissertation.....	16
Chapter 2	Literature review	18
2.1	Introduction.....	18
2.2	Physics based modeling of AlGaIn/GaN HEMT.....	19
2.2.1	Charge Control Model.....	19
2.2.2	Small and Large Signal Modeling.....	21
2.3	Temperature Dependent Modeling.....	22
2.4	AlGaIn/GaN HEMT as CHEMFET.....	24
Chapter 3	Physics Based Model.....	26
3.1	Introduction.....	26
3.2	Nonlinear Charge Control.....	26
3.3	Current-Voltage Characteristics.....	29
3.3.1	Drain Current before Saturation.....	29
3.3.2	Drain Voltage at Saturation.....	31
3.3.3	Drain Current after Saturation.....	32
3.4	Small Signal Parameters.....	34
3.4.1	Transconductance.....	34
3.4.2	Cutoff Frequency.....	35
3.5	Self-Heating Effect.....	36
3.5.1	Calculation of Thermal Impedance.....	37
3.6	Measurement and Simulation Results.....	40
Chapter 4	Temperature Dependent Model.....	43
4.1	Introduction.....	43
4.2	Temperature Dependent Parameters.....	43
4.2.1	Fermi Energy.....	43
4.2.2	Energy band offset.....	44
4.3	Quantum Correction.....	45
4.3.1	Spontaneous and Piezoelectric Polarization.....	45
4.3.2	Mobility.....	46
4.4	Simulation and experimental results.....	47
Chapter 5	AlGaIn/GaN HEMT as Sensor	51
5.1	Introduction.....	51
5.2	Role of Photosystem I Reaction Centers.....	52

5.2.1	Structure of Photosystem I Reaction Center	54
5.3	Immobilization of PS I Reaction Center	55
5.4	AlGaN/GaN CHEMFET	57
5.4.1	Experiment and Results	57
5.5	Model formulation	63
5.6	Discussion	67
Chapter 6	Conclusion and Future Work	69
	Future Works	70
References	71
Vita	76

List of Tables

Table 1.1: Properties of Competing Materials in Power Electronics [1]	3
Table 1.2: High Temperature Electronics Applications of Wide bandgap semiconductors [18]	14
Table 4.1: Values of k_1 , k_2 , and k_3 at different temperatures	44

List of Figures

Figure 1.1: Intrinsic carrier concentration as function of temperature [7].....	4
Figure 1.2: Impurity and electron scattering in MESFET structure [9].....	6
Figure 1.3: AlGaAs-GaAs HEMT structure and its energy band diagram on the right [8]	7
Figure 1.4: Polarization properties of GaN and AlGaN materials [14]	8
Figure 1.5: Formation of 2-DEG at the heterointerface.....	9
Figure 1.6: Polarization versus Al mole fraction [7]	10
Figure 1.7: Trend in (a) power density and (b) total power of AlGaN/GaN HEMT [1] ..	11
Figure 1.8: Fujitsu's developed GaN HEMT amplifier chip [16]	12
Figure 1.9: Power versus frequency chart for various semiconductors	13
Figure 1.10: Power versus frequency requirements for various applications [1]	13
Figure 1.11: Application of CHEMFET	15
Figure 2.1: Equivalent circuit for small signal modeling of AlGaN/GaN HEMT.....	24
Figure 3.1: Schematic of AlGaN/GaN HEMT	28
Figure 3.2: Energy band diagram of AlGaN/GaN HEMT.....	28
Figure 3.3: Schematic of channel layer for AlGaN/GaN HEMT	32
Figure 3.4: Equivalent thermal circuit for self-heating effect.....	37
Figure 3.5: Schematic of an equivalent heat source for the calculation of thermal Impedance	39
Figure 3.6: Temperature profile of a FET.....	39
Figure 3.7: Transfer characteristics of AlGaN/GaN HEMT after saturation ($V_{DS} = 10$ V)	41
Figure 3.8: Simulated and Measured output characteristics of AlGaN/GaN HEMT	41
Figure 3.9: Simulated negative output conductance in saturation region when higher drain-to-source voltages are applied	42
Figure 4.1: Quantum correction (Δd) dependency on temperature.....	46
Figure 4.2: Simulated transconductance of the HEMT with variation of gate-to-source voltage and V_{DS} of 10 V for varying temperature	49
Figure 4.3: Analytical and Measured output characteristics of AlGaN/GaN HEMT at V_{GS} $= 0$ V for varying temperature	49
Figure 0.1: Simulated unity gain cutoff frequency of the HEMT with variation of gate-to- source voltage and V_{DS} of 10 V for varying temperature.....	50
Figure 5.1: Role of reaction centers in photosynthesis (used with permission from Dr. Lee)	53
Figure 5.2: Schematic illustration of the structure and function of an isolated PS I reaction center core antenna complex.....	53
Figure 5.3: The orientation of individual PSI reaction center	56
Figure 5.4: PS I Reaction Centers immobilized on the gate of an AlGaN/GaN HEMT ..	57
Figure 5.5: Kinetic profile of P700+ steady-state formation and reduction	59
Figure 5.6: Absorption spectrum of PS I reaction centers	59
Figure 5.7. (A) Schematic of parallel HEMTs (B) Microphotograph of the HEMT during I-V measurement.....	60

Figure 5.8: Light and dark characteristics of the HEMT ($L = 0.2 \mu\text{m}$, $W = 100\mu\text{m}$) without any external layer and with immobilized PS I reaction centers on the surface. Dotted and solid lines represent dark and light responses, respectively in both cases.	62
Figure 5.9: Change in light (solid) and dark (dotted) characteristics of the HEMT due to immobilization of PS I reaction centers only.	63
Figure 5.10: Schematic of the AlGaN/GaN CHEMFET with PS I reaction centers for analytical modeling (drawn not to scale).	65
Figure 5.11: AFM image of the pure gate Au surface. The roughness of the surface can be understood from the hillocks in the AFM image and RMS roughness was measured as 24.4 nm.	67
Figure 5.12: Calculated numbers of reaction centers with the applied drain-to-source voltages	68

Chapter 1 Introduction

1.1 Introduction

Semiconductor devices are the building blocks of modern electronics. Invention of new semiconductor materials and devices leads to more advanced electronic applications. One of the major demands of advanced electronics which operates and controls functional systems is survival in extreme environments. Silicon (bandgap 1.1 eV) technology could not execute the demand for extreme environment applications due to its intrinsic material properties. Wide bandgap semiconductors (bandgap ~ 3 eV or higher) evolved as the third generation compound semiconductors. These materials possess some special properties, which are exceptionally suitable for high-power, high-frequency and high-temperature device applications.

This chapter describes the motivation and objectives of the research and also summarizes the subsequent chapters.

1.2 Motivation of Research

With the most advanced and mature technology for electronic devices, silicon (Si) based devices can be processed with practically no material defects. However, Si technology has difficulty meeting the demand for some high-power, high-speed and high-temperature applications due to the limitations in its intrinsic material properties. It is

only in the past decade that serious attention has been given to wide bandgap semiconductors for use in device technology.

1.2.1 Wide Bandgap Semiconductors

Wide bandgap materials have intrinsic properties such as high breakdown voltage, lower leakage currents, and higher current density which enable the application of these materials for high-power device operation. Moreover, these materials possess high saturation velocity, large thermal conductivity and excellent thermal stability which make the wide bandgap semiconductor devices most suitable for high-speed and high temperature operation.

Table 1.1 shows the values of different parameters for Si, GaAs and two most widely used wide bandgap semiconductors: SiC and GaN [1]. To combine the effects of these parameters, various figure-of-merits have been reported in the literature. In 1965, Johnson [2] derived a figure of merit, known as Johnson Figure of Merit (JFM) = $\frac{E_c v_s}{2\pi}$ to compare the power-frequency product for low-voltage transistors, where E_c is the critical electric field for breakdown in the semiconductor and v_s is the saturated drift velocity. In 1983, Baliga [3] derived a figure of merit, known as Baliga Figure of Merit (BFM) = $\epsilon\mu E_G^3$, which defines material parameters to minimize the conduction losses in power FET's. Here, μ is the mobility and E_G is the bandgap of the semiconductor. Also, to measure the thermal performance of high power device, a figure-of-merit QF_I has been constructed [4] as the product of $\epsilon\mu E_c^3$ and thermal conductivity λ . Table 1.1 also shows

a comparison of normalized JFM , BFM and QF_1 among the semiconductors of interest discussed earlier. GaN has the highest value for each of these indices, which signifies the greatest prospects of GaN based devices for high-frequency, high-power and high-temperature applications.

The intrinsic carrier concentration of semiconductor is exponentially dependent on temperature [6]:

$$n_i = \sqrt{N_c N_v} \exp\left(-E_G / kT\right) \quad (1.1)$$

where E_G is the bandgap, k is the Boltzmann constant and T is the temperature in Kelvin.

Figure 1.1 shows the intrinsic carrier concentrations of Si, GaAs and various wide bandgap semiconductors for different temperatures. At 0°C (300 K), Si has intrinsic carrier concentration of $1.5 \times 10^{10}/\text{cm}^3$ whereas wide bandgap semiconductors (InN, SiC, GaN or Diamond) show almost zero level of concentration.

Table 1.1: Properties of Competing Materials in Power Electronics [1], [5]

Material	E_g (eV)	μ ($\text{cm}^2/\text{V}\cdot\text{sec}$)	ϵ_r	E_c (kV/cm)	v_s ($10^7 \times$ cm/sec)	λ (W/cm-K)	T_{\max} (°C)	BFM $= \epsilon \mu E_g^3$	JFM $= \frac{E_c v_s}{2\pi}$	QF ₁ $= \lambda \epsilon \mu E_c^3$
Si	1.1	1300	11.4	300	1	1.5	300	1	1	1
GaAs	1.4	5000	13.1	400	1	0.46	300	9.6	3.5	9.4
SiC	2.9	260	9.7	2500	2	1.49	600	3.1	60	300
GaN	3.4	1500	9.5	2000	2.2	1.3	700	24.6	80	910
Diamond	5.45	2200	5.5	10000	2.7	22	2100			198100

As the temperature increases, carrier concentration increases but remains smaller in wide bandgap semiconductors compared to lower energy gap materials.

The thermally generated unwanted carriers contribute to thermal noise which degrades the performance of devices and may destroy the properties of a semiconductor when they become comparable to the concentration of the majority carrier. Hence, the maximum operating temperature of a material is determined by the bandgap of a material as also realized by equation (1.1). Table 1.1 shows the highest operating temperature for GaN which is 700 °C. Therefore, for operation of the devices at elevated temperatures GaN based devices have superior performances compared to other wide bandgap semiconductor (SiC) devices. Diamond possesses a larger bandgap (5.45 eV) which results in better intrinsic properties than GaN. However, diamond technology is not matured enough to exceed the performances of GaN based devices.

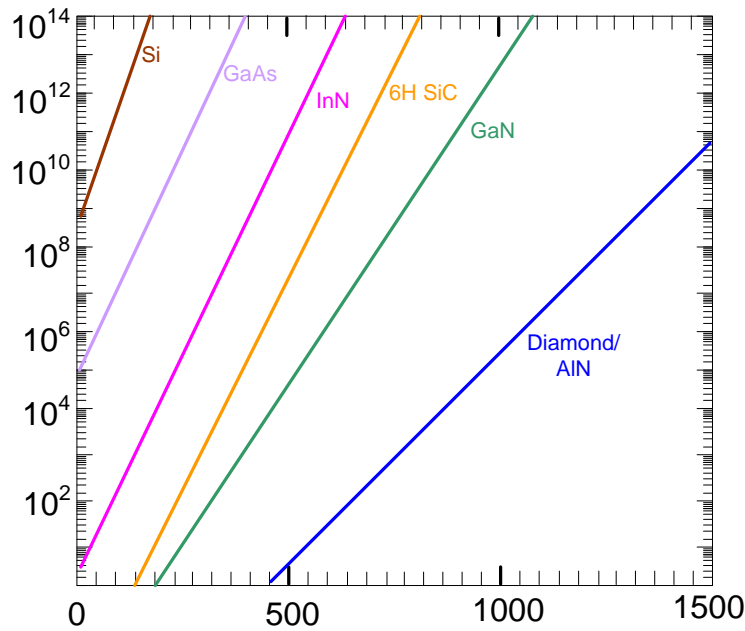


Figure 1.1: Intrinsic carrier concentration as function of temperature [7]

1.3 Introduction to HEMT

Of the various device structures, high electron mobility transistors (HEMT's) show better performances as high-power and high-frequency devices. Capacitive modulation of the channel charges is the basic principle of operation for all the field effect transistor (FET) devices. With this common concept, use of different geometries, different materials and doping profiles results in the variety of FET transistors. Eventually, each type of FET would differ in the confinement of the channel charges and the isolation between the gate and the channel, which would result in a novel device with specific properties. The first HEMT was based on GaAs - AlGaAs superlattices pioneered by L. Esaki and R. Tsu at IBM in the late 1960's [8]. They realized that "high mobilities in GaAs could be achieved if electrons were transferred from the doped and wider bandgap AlGaAs to an adjacent undoped GaAs layer, a process now called modulation doping" [8]. R. Dingle, H. L. Stormer, A. C. Gossard, and W. Wiegmann of AT&T Bell Labs, working independently, demonstrated high mobilities in a GaAs-AlGaAs superlattice in 1978. Realizing the high performance capability of such a structure of the field-effect transistor, researchers of various labs in the United States (Bell Labs, University of Illinois, and Rockwell), and Japan (Fujitsu), and France (Thomson CSF) started working on this device. In 1980, the University of Illinois and Rockwell first fabricated such a device with a reasonable microwave performance, which they named as modulation-doped FET or MODFET. The same year researchers at Fujitsu reported the results for a device with a 400-pm gate. They called the device "high electron mobility transistor" or HEMT. Thereafter, Thomson CSF and Bell Labs followed calling their realizations a "two-dimensional

electron gas FET” or TEGFET, and “selectively doped heterojunction transistor” or SDHT, respectively [8].

In conventional metal-semiconductor FET’s (MESFET’s), the donor impurities generate the electrons (carriers) and reside in the same space/layer with the electrons. As a result, the conducting electrons start colliding with the impurities as shown in Figure 1.2. For higher speed, more current is required which necessitates larger concentration of electrons. This leads to more electron-donor interaction, called ionized impurity scattering.

Also thinner channel layers and higher electron concentrations are required for smaller FET size. The isolation of large electron concentration with donors can be obtained by the heterojunctions. A heterojunction is formed between two different bandgap materials such as AlGaAs and GaAs. The donors are introduced only into the larger bandgap (AlGaAs) material [10], [11]. The electrons originally introduced into the larger bandgap layer (AlGaAs) diffuse to the lower energy (GaAs) layer where they remain confined due to the energy barrier at the heterointerface as illustrated by the band diagram in Figure

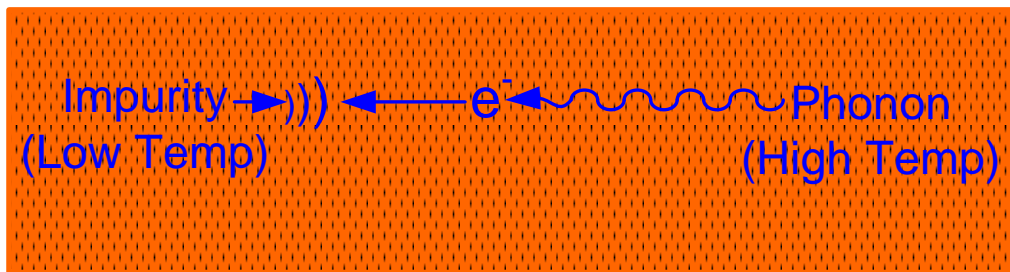


Figure 1.2: Impurity and electron scattering in MESFET structure [9]

1.3. Thus, a 2-dimensional electron gas (2-DEG) is formed at the heterointerface very close to the gate, which leads to very high electron mobilities and large electron velocities at very small values of drain voltage [9].

1.4 GaN HEMT Technology

In 1993, Asif Khan *et al.* first demonstrated a HEMT based on AlGaN and GaN heterojunctions [12]. Since then much progress has been made for the achievement of better performances of AlGaN/GaN HEMT. AlGaN/GaN exhibits improved ratings for power and frequency applications compared to AlGaAs/GaAs HEMT. This is due to the superior intrinsic properties of GaN material compared to GaAs as evident from Table 1.1 and also due to the polarization effects dominant in AlGaN and GaN materials. GaN has both Zincblende and Wurtzite crystalline forms. It is normally grown on the Ga-face, along its c-axis. It has a substantial spontaneous electrical polarization perpendicular to the hexagonal plane, and in the direction down into the Ga-face surface as shown in Figure 1.4. When $\text{Al}_x\text{Ga}_{1-x}\text{N}$ is grown on GaN, larger electrical polarization results in the

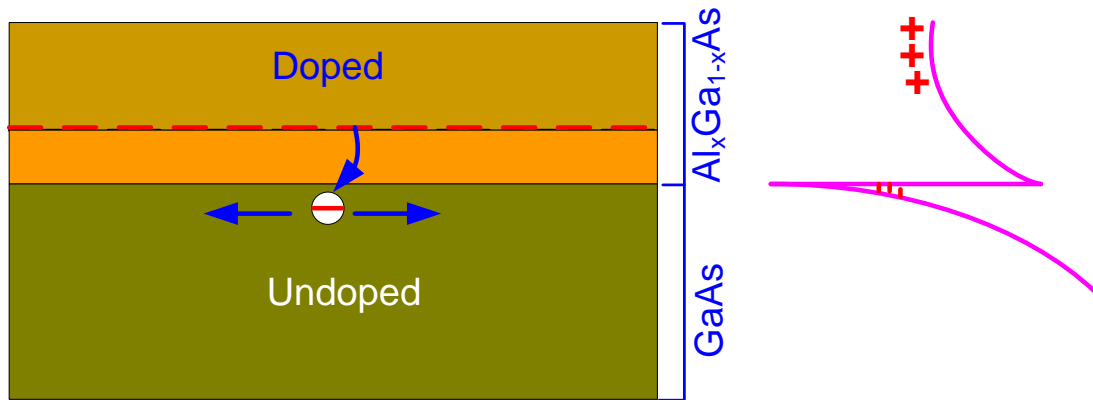


Figure 1.3: AlGaAs-GaAs HEMT structure and its energy band diagram on the right [8]

same direction. $\text{Al}_x\text{Ga}_{1-x}\text{N}$ has a smaller lattice constant, so that the two-dimensional tension causes a piezoelectric effect which adds to the spontaneous polarization [13]. The total electrical polarization between the pseudomorphic $\text{Al}_x\text{Ga}_{1-x}\text{N}$ top barrier layer and the GaN channel layer is obtained by the algebraic sum of individual components as $P_T = P_{SP}(\text{AlGaN}) - P_{SP}(\text{GaN}) + P_{PE}(\text{AlGaN})$. A positive sheet charge density (σ) appears due to the net polarization effect, which causes an accumulation of electrons at the interface and thus forms the 2-DEG (Figure 1.5). Thus, even without any intentional doping in the AlGaN layer, a high charge density (Figure 1.6) channel is formed at the heterointerface.

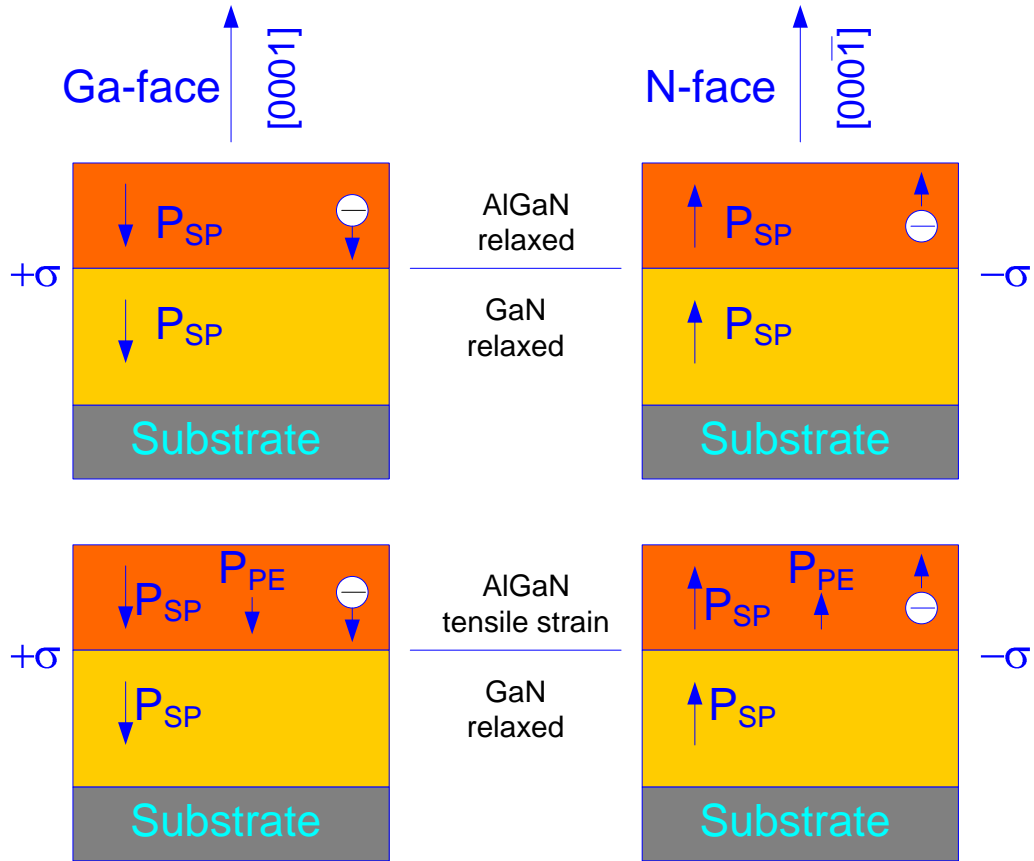


Figure 1.4: Polarization properties of GaN and AlGaN materials [14]

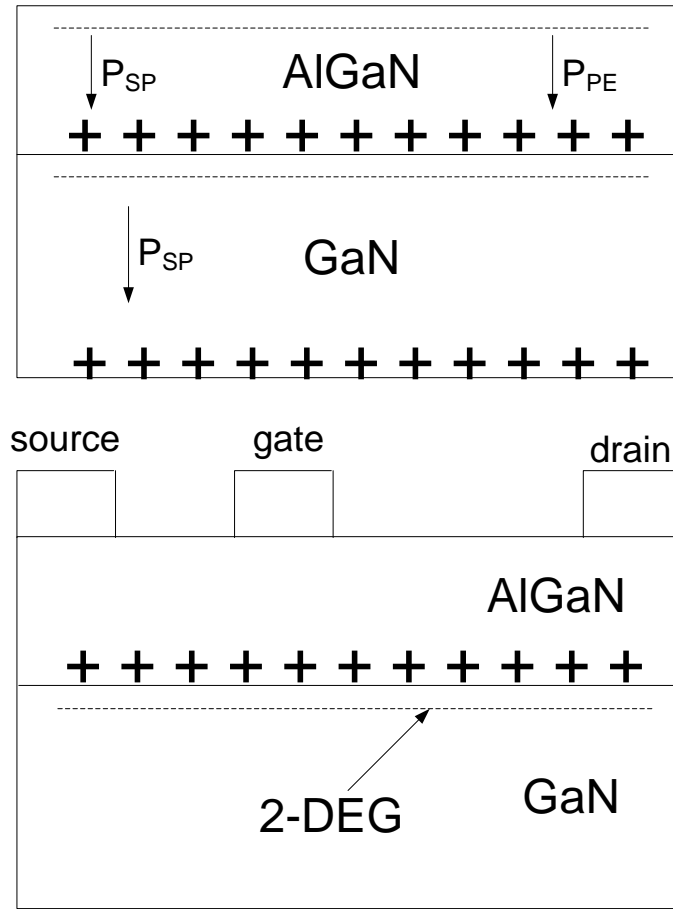


Figure 1.5: Formation of 2-DEG at the heterointerface

Especially in wurtzite AlGaAs/GaN based transistor structures; the piezoelectric polarization of the strained top layer is more than five times larger as compared to that of AlGaAs/GaAs structures, leading to a significant increase of the sheet carrier concentration at the interface [14].

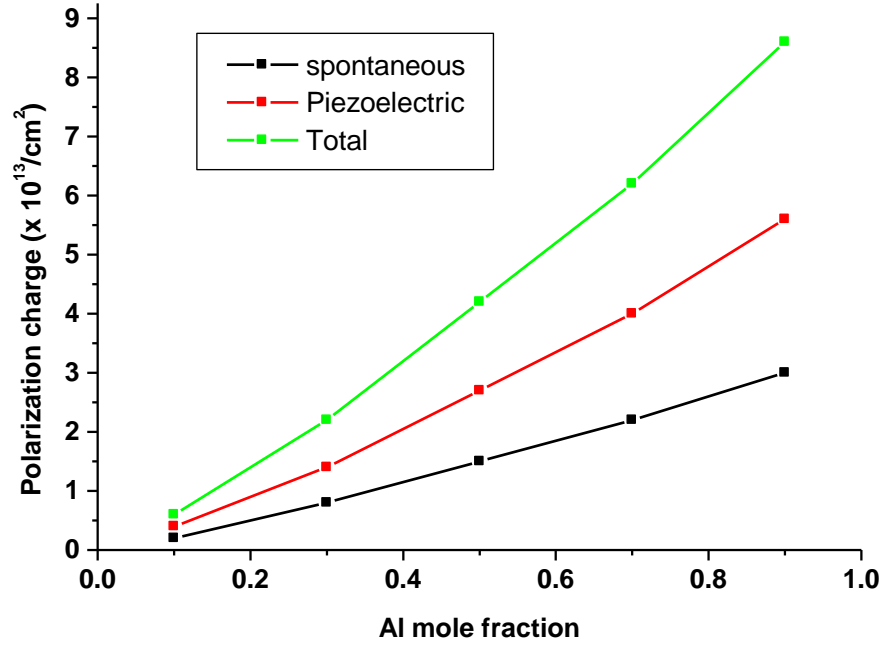


Figure 1.6: Polarization versus Al mole fraction [7]

1.4.1 Prospects of GaN HEMT

AlGaIn/GaN HEMT has been an intense interest of research due to great potential of the material system for high-power and high-frequency applications [15]. With the rapid increase in 3G mobile subscribers, a large-capacity and high-speed system is becoming more crucial. To achieve such a system a power amplifier with higher output power and high linearity for 3G base stations is vital. Such an amplifier should be capable of simultaneously amplifying multiple channels while efficiently converting power into radio frequency signals. Thus, the amplifier will reduce the power consumption and require simpler cooling system resulting in smaller and cost-efficient base stations.

Conventional amplifiers composed of Si DMOS transistors or GaAs transistors require power-combining circuits due to the small output power of each transistor. As a result, the amplifier is larger in size and there is an increased loss in power.

Figure 1.7 shows the power density and total power of AlGaIn/GaN HEMT achieved by different companies and laboratories from 1992 to 2002 [1] on both SiC and Sapphire substrates. As the power increases, channel temperature rises depending on the thermal resistance of the device. Thermal conductivity of the substrate dominates determining the thermal impedance of a device. SiC has higher thermal conductivity (4.5 W/cm-K) than Sapphire (0.42 W/cm-K) but the former is more expensive than later. Hence, a prudent choice is required for the selection of substrate to optimize the cost and the performance of a system.

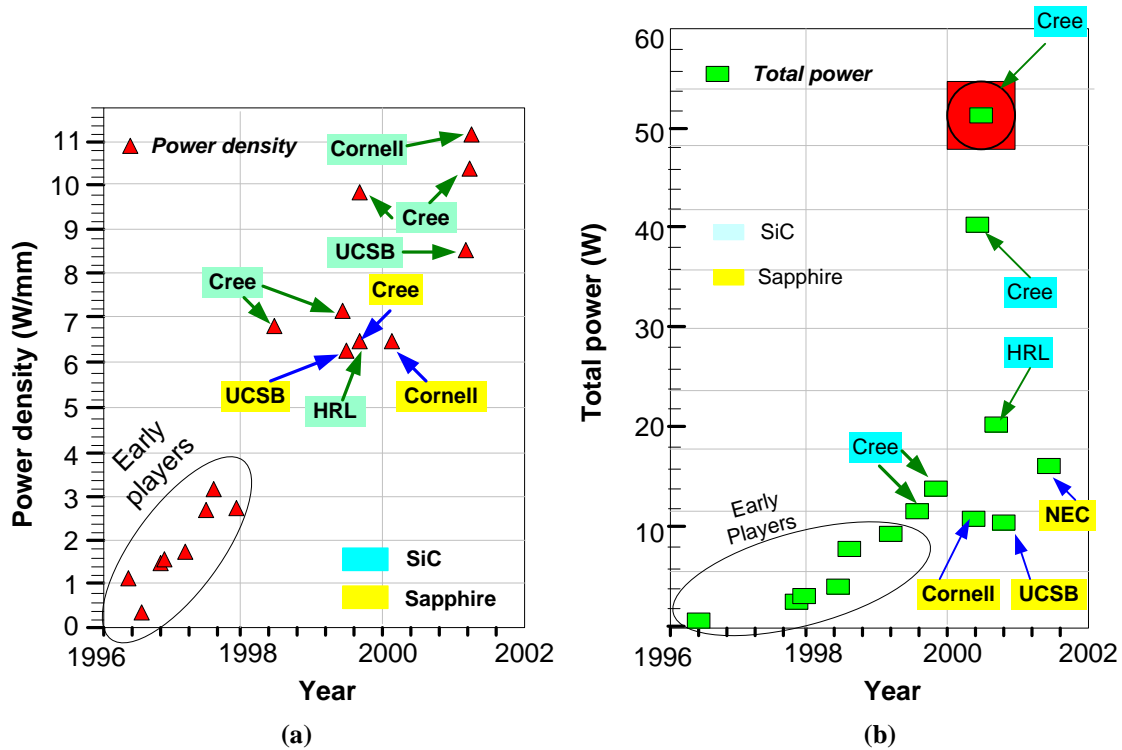


Figure 1.7: Trend in (a) power density and (b) total power of AlGaIn/GaN HEMT [1]

In 2003, Fujitsu Laboratories Ltd. achieved “breakthrough output with Gallium Nitride HEMT amplifier” [16]. Fujitsu fabricated GaN HEMT amplifier (shown in Figure 1.8) with an output of 174 W at 63 V high voltage operations with drain efficiency of 40% and thus fulfilling the requirements for base stations. In 2006, NEC Corporation developed high-power GaN transistor amplifier for 3G base stations [17]. NEC reported operating voltage of 45V and peak output power of 400W for WCDMA signal (2.14 GHz), drain efficiency of 25% at average output power of 60W. Figure 1.9 shows the power versus frequency domain for GaN with other semiconductors. Based on the power and frequency prospects, possible fields of applications for AlGaIn/GaN HEMT are mentioned in Figure 1.10. Table 1.2 shows the approximate operating temperatures for various applications of wide bandgap semiconductors including GaN. Therefore, high temperature operation of AlGaIn/GaN HEMT is required to target various applications.

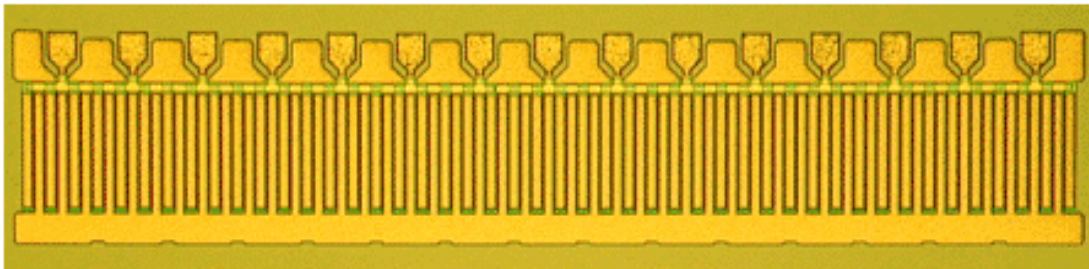


Figure 1.8: Fujitsu's developed GaN HEMT amplifier chip [16]

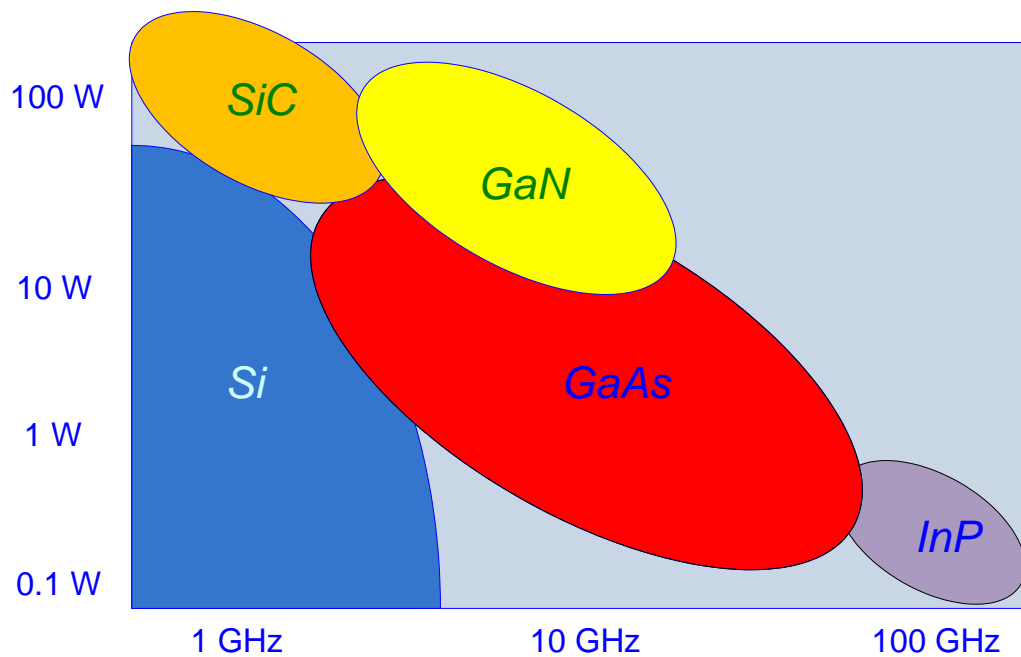


Figure 1.9: Power versus frequency chart for various semiconductors

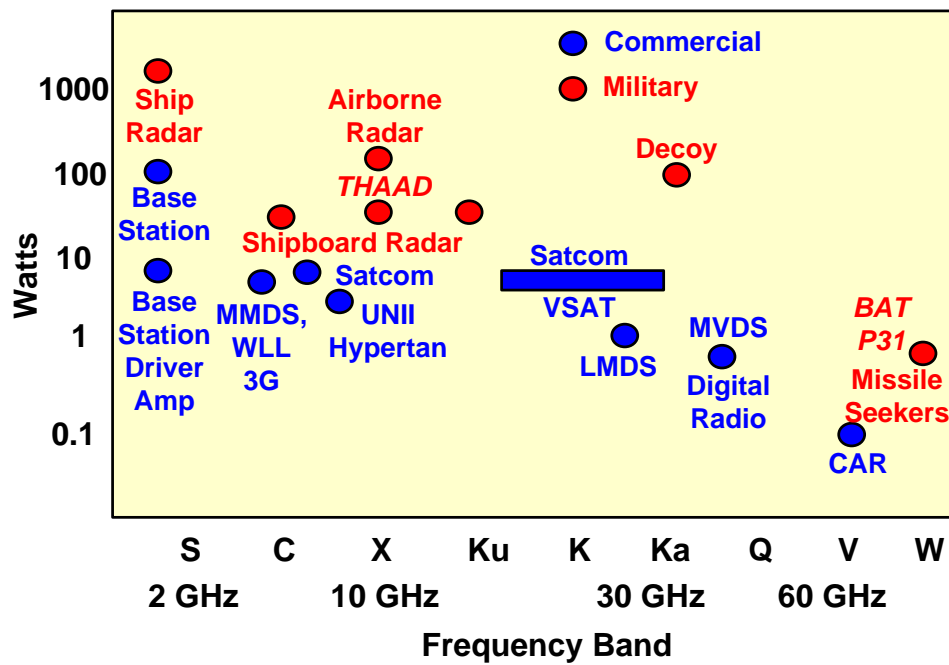


Figure 1.10: Power versus frequency requirements for various applications [1]

Table 1.2: High Temperature Electronics Applications of Wide bandgap semiconductors [18]

High Temperature Electronics Application	Peak Ambient	Peak power	Current Technology	Future Technology
Automotive				
Engine Control Electronics	150 °C	< 1 kW	BS & SOI	BS & SOI
On-cylinder Exhaust pipe	600 °C	< 1 kW	NA	WBG
Electric Suspension & Brakes	250 °C	> 10 kW	BS	WBG
Electric/Hybrid Vehicle PMAD	150 °C	> 10 kW	BS	WBG
Turbine Engine				
Sensors, Telemetry, Control	300 °C	< 1 kW	BS & SOI	SOI & WBG
	600 °C	< 1 kW	NA	WBG
Electric Actuation	150 °C	> 10 kW	BS & SOI	WBG
	600 °C	> 10 kW	NA	WBG
Spacecraft				
Power Management	150 °C	> 1 kW	BS & SOI	WBG
	300 °C	> 10 kW	NA	WBG
Venus & Mercury Exploration	550 °C	~ 1 kW	NA	WBG
Industrial				
High Temperature Processing	300 °C	< 1 kW	SOI	SOI
	600 °C	< 1 kW	NA	WBG
Deep-Well Drilling Telemetry				
Oil and Gas	300 °C	< 1 kW	SOI	SOI & WBG
Geothermal	600 °C		NA	WBG

1.4.2 Potential of AlGaIn/GaN HEMT as CHEMFET

Field effect transistor technology has evolved into a popular device called CHEMFET ([19]-[21]) for the detection and the characterization of biomolecules due to amplification advantages and simpler imprint methods. Due to higher current and greater sensitivity, AlGaIn/GaN has larger potential as CHEMFET (Figure 1.11) compared to other field effect transistors. The gate surface of a field effect transistor is chemically modified for the immobilization of the target molecules. Upon immobilization, the electric field

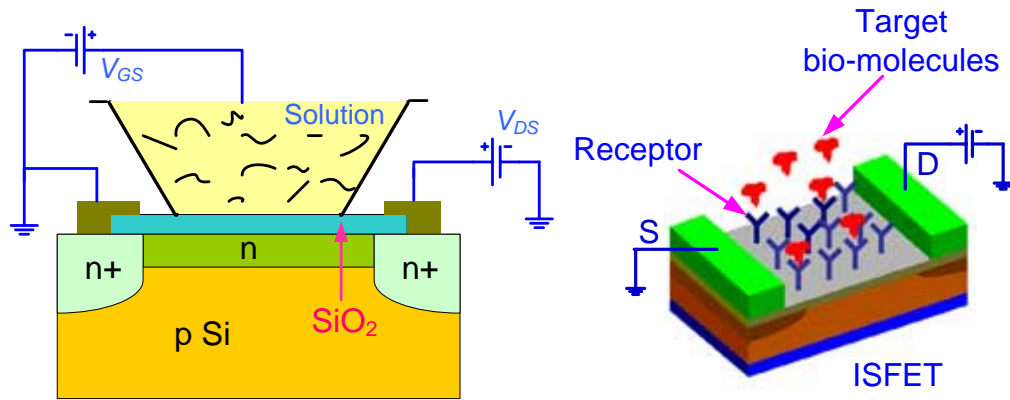


Figure 1.11: Application of CHEMFET

distribution of the transistor changes, which in effect modulates the channel charges and therefore, the output current of the transistor.

1.5 Research Objectives

As discussed in the previous sections, AlGaIn/GaN HEMT is preferable candidate for high speed-high power applications operating at different temperatures. To predict and optimize device behavior, analytical model is a quick solution. A very few temperature dependent analytical models of AlGaIn/GaN HEMT exists in literature. Most of the works published discussed temperature dependent characteristics of the HEMT based on experiment. Some of the works showed temperature dependent modeling of the HEMT based on nonlinear cubic fit Curtice model, Volterra series etc. Some authors only studied temperature dependent device parameters such as mobility, saturation velocity by Monte Carlo simulation. Hasina Huq [22] developed a temperature dependent analytical model based on simplified physics of the device. Moreover, the author [22] did not validate the model with high temperature data. Therefore, physics based accurate temperature

dependent model for different operating conditions is required to exploit the superior performances of AlGa_N/Ga_N HEMT. Keeping this in mind, this research has been performed to address the following aspects of AlGa_N/Ga_N HEMTs:

- a) Development of nonlinear charge control based DC model
- b) Development of small signal and large signal model
- c) Development of temperature dependent model based on the physics based model

AlGa_N/Ga_N HEMT has also great potential to be used as CHEMFET. Using the the physics based model, a mathematical formulation has been achieved for AlGa_N/Ga_N HEMT based bimolecular sensor. In this regard, following work has been done:

- d) Investigation of the feasibility of AlGa_N/Ga_N HEMT as sensors
- e) Derivation of an analytical model to count the number of photosystem I (PS I) reaction centers of effective orientation on the gate of an AlGa_N/Ga_N HEMT

1.6 Outline of Dissertation

Chapter 2 discusses the previous work on the fundamental physics and modeling of HEMT. Various temperature dependent modeling found in literature have also been elaborated. The work on AlGa_N/Ga_N HEMT based sensor has also been discussed.

In chapter 3, the mathematical formulation of analytical model for DC, small signal and large signal characteristics of AlGa_N/Ga_N HEMT have been described. The simulated characteristics have been compared with the experimental data at room temperature.

In chapter 4, temperature dependent modeling of AlGa_N/Ga_N HEMT has been derived from the physics based model developed in chapter 3. The simulated temperature dependent characteristics have been compared with the experimental data for temperature of 300 K to 500 K.

Chapter 5 describes the application of AlGa_N/Ga_N HEMT as a sensing and characterization device for bio molecules. An analytical model has been developed to characterize PS I reaction centers using the HEMT.

Chapter 6 discusses the original contribution to this research, draws the conclusion and presents an outline for future work.

Chapter 2 Literature review

2.1 Introduction

Despite the presence of large defects, GaN based device technology has advanced a lot due to its excellent electrical properties in application of high-power, high-frequency and high-temperature fields. Due to wider bandgap (3.4 eV), GaN based HEMTs have higher breakdown voltages and lower leakage currents compared to most commonly used Si and GaAs based devices. Continuous channel of two-dimensional electron gas (2-DEG) present at the hetero-interface of GaN and AlGaIn layers results in lower on-resistance in these power HEMTs. High Polarization field results in larger 2-DEG density and hence, larger current output in the AlGaIn/GaN HEMTs. Higher value of saturation velocity ($\sim 2.5 \times 10^7$ cm/s) facilitates high frequency operation and larger bandgap minimizes the adverse effects of high temperature operations.

Realizing the greater of potential applications of GaN based devices; researchers have been trying to model the device from different perspectives in order to get a quick prediction of the characteristics of the devices or to optimize the performances before sending the device design for fabrication. As a result, a good volume of literature on the modeling of AlGaIn/GaN HEMT has been found. In this chapter, some of the previous work has been described for the physics based modeling of AlGaIn/GaN HEMT. In addition, up to date literature of temperature dependent modeling has been briefly illustrated.

This research also includes modeling of the effective number of charges on the surface of an AlGaIn/GaN HEMT based sensor or CHEMFET. AlGaIn/GaN based heterostructures have already been investigated as sensors. In this chapter, literature on GaN based sensors has also been elucidated.

2.2 Physics based modeling of AlGaIn/GaN HEMT

The physics based model of AlGaIn/GaN HEMT is based on the charge control theory of gate potential, which is also the basic working theory for any field-effect transistor.

2.2.1 Charge Control Model

The HEMT charge control model has been first developed by D. Delagebeaudeuf and N. T. Linh [23]. Due to heterojunction, a 2-DEG is formed at the heterointerface of a HEMT. The analytical expression for the sheet carrier density at the heterointerface of an AlGaAs/GaAs HEMT has been expressed as [23],

$$Q_s = qn_s = \frac{\epsilon_2}{d_2} (\phi_G - V_{off} - E_F) \quad (2.1)$$

where n_s is 2-DEG density, ϵ_2 is the permittivity of the higher bandgap (barrier) material, d_2 is the distance between the 2-DEG and the Schottky gate, V_G is the applied gate voltage and V_{off} is ‘off voltage’ which annihilates the 2-DEG and given by

$$\begin{aligned} V_{off} &= \phi_M - \Delta E_c - V_{p_2} - \frac{d_2}{\epsilon_2} Q_i \\ V_{p_2} &= \frac{qN_2}{2\epsilon_2} (d_2 - e) \end{aligned} \quad (2.2)$$

e is the thickness of spacer layer between the doped layer and the 2-DEG, Q_i is the interface states charge. In this paper [23], E_F , which is function of gate voltage V_G , has been neglected compared to the other terms and thus equation (2.1) has been approximated as,

$$Q_s = \frac{\epsilon_2}{d_2} (V_G - V_{off}) \quad (2.3)$$

which describes the linear relationship between the sheet carrier density and the gate voltage. Based on this linear charge-control, analytical expressions for the current-voltage characteristics of the HEMT have been developed [25] - [30].

An important physical aspect for the development of the analytical expressions of the current-voltage and capacitance-voltage characteristics of HEMTs is the variation of the sheet carrier concentration (n_s) in the 2-DEG as a function of the applied gate voltage (V_G). The simple analytical expressions for n_s vs V_G , are accurate only for a limited range of values of n_s , ($> 5 \times 10^{11}/\text{cm}^2$) [31]. For the modeling near the threshold region of operation of HEMTs, the linear charge control is not accurate. A. Shey and W. H. Ku [32] showed an analytical model for the prediction of current-voltage characteristics assuming an approximated relationship between Fermi level E_F and n_s ,

$$E_F = E_{F0} + \gamma n_s^{2/3} \quad (2.4)$$

where E_{F0} is equilibrium Fermi level and γ is a constant linking the 2-DEG carrier density with the longitudinal quantized energy. This approximation is valid as long as the device is not operated in the deep subthreshold region. N. Dasgupta and A. Dasgupta [33] formulated an analytical expression of n_s vs V_G , valid for operation at different

temperatures, which is shown to be accurate from subthreshold to high conduction regions of device operation. In the model [33], E_F is expressed as a function of n_s by a simple polynomial equation,

$$E_F = k_1 + k_2 n_s^{1/2} + k_3 n_s \quad (2.5)$$

where k_1 , k_2 , k_3 are temperature dependent constants. But in this work, no closed form expression for the current-voltage characteristics of the HEMT has been shown which uses the nonlinear relation between n_s and V_G .

In this dissertation work, nonlinear relation between E_F and n_s as defined by equation (2.5) has been undertaken to derive a new formulation of accurate current-voltage characteristics.

2.2.2 Small and Large Signal Modeling

AlGaIn/GaN has been fabricated and measured for small and large signal performances. Continuous-wave (CW) power densities as high as 11.2 W/mm have been demonstrated for the AlGaIn/GaN devices at 10 GHz [34]. In the *Ku*-band, a GaN monolithic microwave integrated circuit (MMIC) operating at 16 GHz has recently been demonstrated with the total CW output power of 24.2 W [35]. Asif Khan's group [36] has reported GaN/AlGaIn HEMT operation in the *K*-(18 - 27 GHz) and *Ka*-(27 - 40 GHz) bands. When biased and tuned for the maximum output power, the device showed a total output power of 1.6 W with an associated power-added efficiency (PAE) of 27% and

gain of 10 dB. The corresponding power density was 3.2 W/mm [36]. J. S. Moon *et al.* [37] reported power density > 6 W/mm at 20 GHz.

To predict the high frequency and large signal performances, research has been done to develop an analytical model of the devices. The intrinsic small signal model has two components. One is the intrinsic DC current source, I_{DS} and the other comprises of extracted capacitances and resistances of the device as shown in Figure 2.1. For connecting the device to the outer circuits, pad capacitance and bond wire inductance are incorporated for complete small signal modeling [39], [40]. For large signal modeling, the current dispersion due to self-heating [42] and trapping of carriers [42] are incorporated with the intrinsic DC model.

2.3 Temperature Dependent Modeling

The high power operation of a device is limited by the increase in device junction temperature. Due to high mobility and presence of high density sheet carriers, AlGaIn/GaN HEMT is the most suitable for high power applications. The channel temperature increases with the increase in output power and consequently, performance of the device degrades due to spurious effects of the elevated temperature. Also, for application in extreme environment sensing and telemetry AlGaIn/GaN HEMTs are require high power and high frequency operation of at higher temperatures. Mobility degradation, change in threshold voltage, generation of leakage currents are the common physical phenomena which affect the device characteristics. To find the temperature limit

of a device, analytical model is the quick solution to predict the device performances at the temperature required for a specific application. Physics based temperature dependent modeling is advantageous to predict and optimize the device performance. Most of the published work to date has focused on the experimental results for the characteristics of AlGaIn/GaN HEMT at different temperatures [44], [45]. Some work has been published studying the Monte Carlo simulation for the device parameters such as mobility, saturation velocity [46]. Y. Chang *et al.* showed temperature dependent static characteristics of AlGaIn/GaN HEMT based on a numerical technique of solving Schrödinger and Poisson equations self-consistently [47]. There are few physics based models. A. Ahmed *et al.* published a temperature dependent model based on Volterra series [48]. The authors derived the temperature dependent small signal parameters using Volterra series. This model does not provide full insight to the device physics at varying temperature. H. F. Huq [22] showed a temperature dependent charge control model of AlGaIn/GaN HEMT. The author did not consider the variation of Fermi energy as function of gate voltage, polarization effects and channel-length modulation in the charge control model. Also, for temperature dependent modeling, self-heating effect has not been considered in this work [22].

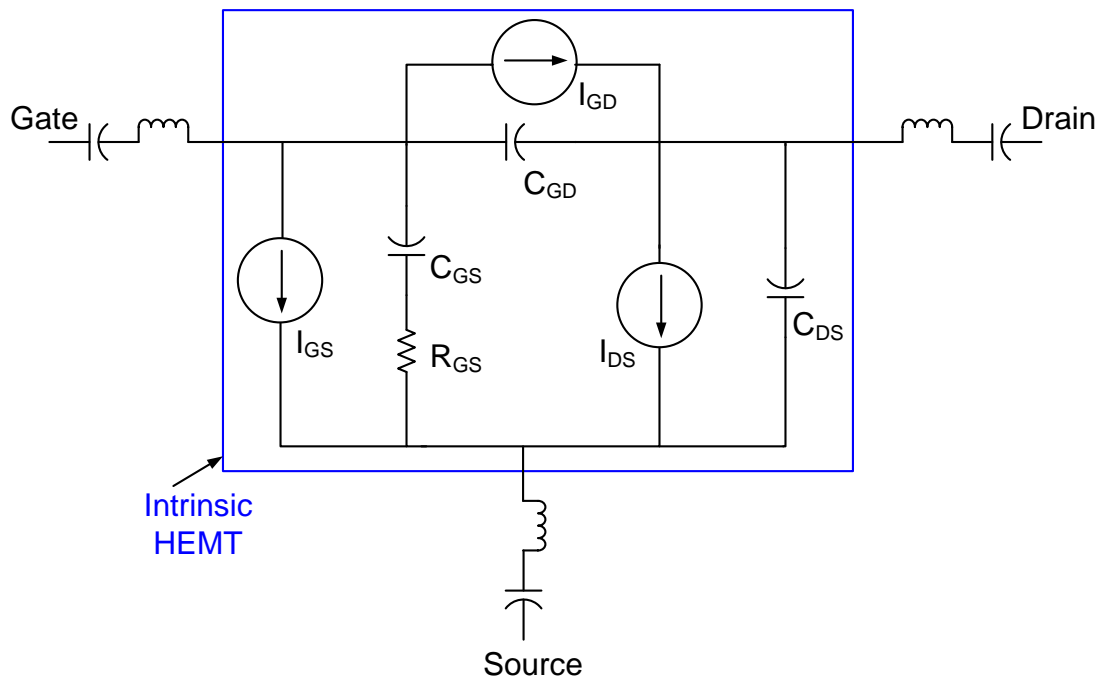


Figure 2.1: Equivalent circuit for small signal modeling of AlGaN/GaN HEMT

2.4 AlGaN/GaN HEMT as CHEMFET

Recently field-effect transistor based CHEMFETs for the detection and the characterization of molecules have become very popular due to the simpler imprint technique and amplification advantages. Using CHEMFET technique, various types of liquids including bio-fluids, gaseous substances have been detected. Among the different FET structures, AlGaN/GaN HEMT has the highest potential for working as sensors as diamond technology is a long way from reaching its maturity. Imprinting biomolecules for the construction of electrical devices has been a significant challenge due to temperature and resolution constraints of the growth processes. Several approaches for fabrication of two-terminal electrical devices using molecules have been reported [49]-[53]. In order to place contacts across a single molecule, an electrode pair with a gap

equivalent to the nanometer size of the molecule is required. A lithographically fabricated mechanically controlled break (MCB) junction has been demonstrated for construction of an electrode pair with tunable distance [50]. The electrical break junction (EBJ) was another technique employed for this purpose [51]. The success of these methods depends on creating a contact across a single molecule or between the molecules. Hence, these are quite nondeterministic methods due to the constraint of the size of a molecule. The concept of molecules sandwiched between two metal films [53] is also not appropriate. Molecules are non-deterministically or discretely immobilized on the substrate metal which leaves the chances of short circuits during the growth of the second metal. Therefore, realizing all these difficulties for constructing an electrical device of biomolecules, researchers have focused on CHEMFET based characterization technique. In this research, AlGaIn/GaN HEMT has been used for the detection and the characterization of Photosystem I reaction centers.

Chapter 3 Physics Based Model

3.1 Introduction

This chapter describes the formulation of an analytical model for the AlGaIn/GaN HEMT. The model has been developed considering the nonlinear control of gate potential on sheet carrier density. Due to the nonlinear nature of the charge control equation, mathematical complexity arises in the current-voltage relationship, which has been simplified based on realistic assumption. The relationship between drift velocity and electric field for GaN channel has been approximated by an empirical equation. Both the spontaneous and the piezoelectric polarization induced charges at the AlGaIn/GaN heterointerface have been considered. The effects of channel length modulation in the saturation region have been included. Transconductance, g_m and unity-gain cutoff frequency, f_T have been calculated to derive the small signal model of the AlGaIn/GaN HEMT. Self-heating effects have been considered to incorporate large signal nonlinearity.

3.2 Nonlinear Charge Control

The structure of AlGaIn/GaN HEMT is shown in, Figure 3.1, and the corresponding energy band diagram are depicted in Figure 3.2. The expression for sheet carrier density is written as [30],

$$n_s(x) = \frac{q\epsilon_2}{q^2d + \epsilon_2a} \left(V_G - V(x) - V_{TO} \right) \quad (3.1)$$

where V_G , $V(x)$ and V_{TO} represent applied gate voltage, channel potential at x and threshold voltage, respectively, d is $(d_d + \Delta d)$ with the thickness of AlGaIn (barrier) layer, d_d and the offset distance of the 2-DEG density from the hetero-interface, Δd and ϵ_2 and a are permittivity of the barrier layer and the quantum well shape factor, respectively. For the nonlinear charge control as described in chapter 2, the threshold voltage V_{TO} is defined as,

$$V_{TO} = V_{off} + E_F \quad (3.2)$$

where V_{off} is given by,

$$V_{off} = \phi_m - \frac{\Delta E_c}{q} - \frac{q\sigma d_d}{\epsilon_2} \quad (3.3)$$

ϕ_m is the Schottky barrier height of gate, σ is the charge density due to spontaneous and piezoelectric polarizations and ΔE_c is the conduction band offset at the heterointerface.

Using equations (2.5) and (3.2) in equation (3.1), n_s can be redefined as,

$$n_s = \frac{q\epsilon_2}{q^2d + \epsilon_2a} \left(V_G - V(x) - V_{off} - k_1 - k_2n_s^{1/2} - k_3n_s \right) \quad (3.4)$$

This is a standard quadratic equation in n_s and the solution of this equation yields,

$$n_s(x) = \frac{\left[B \pm \sqrt{B^2 - 4AC} \right] - \left(V_G - V(x) - V_{off} \right)}{4A^2} \quad (3.5)$$

where $C = \frac{q\epsilon_2}{q^2d + \epsilon_2a}$, $A = 1 + k_3C$, $B = k_2C$.

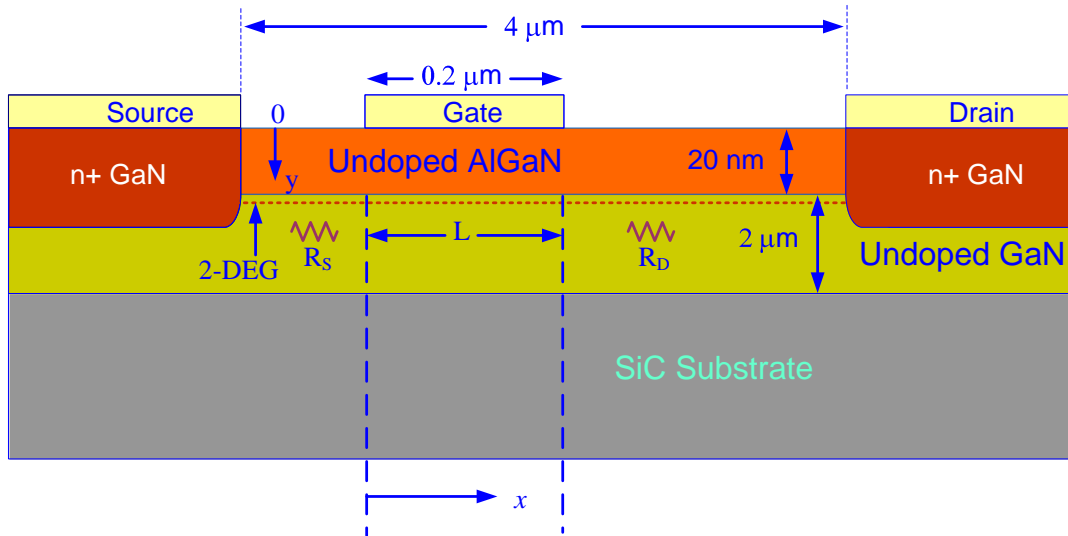


Figure 3.1: Schematic of AlGaN/GaN HEMT

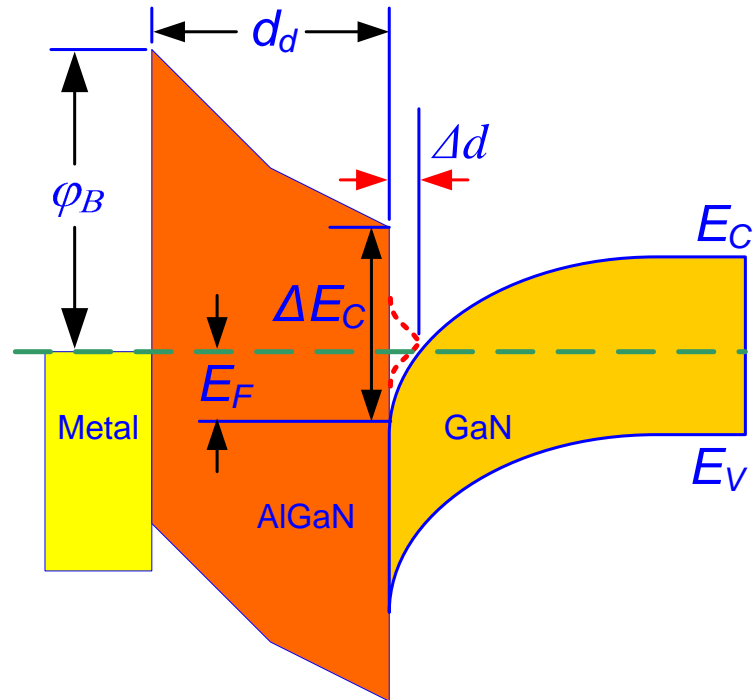


Figure 3.2: Energy band diagram of AlGaN/GaN HEMT

3.3 Current-Voltage Characteristics

The drain current is given by [54],

$$I_D = qn_s(x)Zv(x) \quad (3.6)$$

where Z is the gate width and $v(x)$ is the electron drift velocity. The relationship between the drift velocity and the electric field used by in this work is expressed as [29],

$$v(x) = \frac{v_s E}{\sqrt{E^2 + (v_s / \mu_0)^2}} \quad (3.7)$$

where v_s is the saturation drift velocity and μ_0 is the low-field mobility.

Substituting equations (3.5) and (3.7) in (3.6),

$$I_D = G_o \frac{R^2}{4A^2} \frac{E}{\sqrt{E^2 + \xi_c^2}} \quad (3.8)$$

where $G_o = qZv_s$, $E_c = \frac{v_s}{\mu}$, and $R = -B \pm \sqrt{B^2 - 4AC}$ $\left\{ \begin{array}{l} \text{for } V_G - V(x) - V_{off} \geq 0 \\ \text{for } V_G - V(x) - V_{off} < 0 \end{array} \right.$

3.3.1 Drain Current before Saturation

Writing $E(x) = -\frac{dV(x)}{dx}$ in equation (3.8),

$$dV(x) \left[\frac{1}{16} \left(\frac{G_o}{I_D} \right)^2 \frac{R^4}{A^4} - 1 \right]^{1/2} = -\xi_c dx \quad (3.9)$$

Now R can be newly defined by $-B + \sqrt{t}$, which transforms equation (3.9) into,

$$dt(x) \left[(-B + \sqrt{t})^4 - 1 \right]^{1/2} = -4AC\xi_c dx \quad (3.10)$$

Integrating equation (3.10) from $x = 0$ to $x = L$,

$$\int_0^L dt(x) \left[P \left(B + \sqrt{t} \right) - 1 \right]^{1/2} = -4AC\xi_c dx \quad (3.11)$$

where $t = B^2 - 4AC \left(\frac{1}{16A^4} \left(\frac{G_o}{I_D} \right)^2 - V_G - V_{off} - V(x) \right)$, and $P = \frac{1}{16A^4} \left(\frac{G_o}{I_D} \right)^2$

Let,

$$\sec^{-1} \left(\sqrt{P} (-B \pm \sqrt{t}) \right) = \theta \quad (3.12)$$

Hence,

$$dt = \frac{\pm \sec^{1/2} \theta \tan \theta}{P^{1/4}} \left(\pm \frac{\sec^{1/2} \theta}{P^{1/4}} \pm B \right) d\theta \quad (3.13)$$

Using variable transformation from t to θ , equation (3.11) can be rewritten as,

$$\frac{1}{P^{1/2}} \int_{\theta_0}^{\theta_L} \sec \theta \tan^2 \theta d\theta + \frac{B}{P^{1/4}} \int_{\theta_0}^{\theta_L} \sqrt{\sec \theta} \tan^2 \theta d\theta = -4AC\xi_c L \quad (3.14)$$

where

$$\theta_0 = \sec^{-1} \left[\sqrt{P} \left(B + \sqrt{t_0} \right) \right], t_0 = B^2 - 4AC \left(\frac{1}{16A^4} \left(\frac{G_o}{I_D} \right)^2 - V_G - V_{off} - I_D R_s \right) \quad (3.15)$$

$$\theta_L = \sec^{-1} \left[\sqrt{P} \left(B + \sqrt{t_L} \right) \right], t_L = B^2 - 4AC \left(\frac{1}{16A^4} \left(\frac{G_o}{I_D} \right)^2 - V_G - V_{off} - V_D + I_D R_D \right) \quad (3.1)$$

$$II_1 = \int_{\theta_0}^{\theta_L} \sec \theta \tan^2 \theta \cdot d\theta = \left[\frac{\sin^3 \theta}{2 \cos^2 \theta} + \frac{1}{2} \sin \theta - \frac{1}{2} \ln \left| \sec \theta + \tan \theta \right| \right]_{\theta_0}^{\theta_L} \quad (3.16)$$

$$II_2 = \int_{\theta_0}^{\theta_L} \sqrt{\sec \theta} \tan^2 \theta \cdot d\theta = \left[\frac{2}{3} \sec^{1/2} \theta \left(\tan \theta - 2 \cos^{1/2} \theta \cdot F \left(\frac{\theta}{2}, m \right) \right) \right]_{\theta_0}^{\theta_L} \quad (3.17)$$

where F is *incomplete Elliptic Integral* which requires large computation time and may encounter convergence problem during numerical evaluation. To avoid this integral, truncated series is obtained based on the following condition:

At saturation, $\theta = 0, \cos\theta = 1$. This is derived in the following section.

Hence, $|z| = \cos\theta < 1$ and the integral in equation (3.18) can be transformed in z as

follows:

$$\begin{aligned} \int_{\theta_0}^{\theta_L} \sqrt{\sec\theta} \tan^2 \theta d\theta &= \int_{z_0}^{z_L} z^{-5/2} \sqrt{1-z^2} dz \\ &= \left[\frac{2}{3} z^{-3/2} + z^{1/2} + \frac{1}{20} z^{5/2} + \frac{1}{72} z^{9/2} + \frac{5}{832} z^{13/2} \right]_{z_0}^{z_L} \end{aligned} \quad (3.18)$$

where $z_0 = \cos\theta_0$ and $z_L = \cos\theta_L$

Equations (3.14), (3.17) and (3.19) yield I - V characteristics before saturation i.e., when

$V_D < V_{D,sat}$ where $V_{D,sat}$ is the drain-saturation-voltage.

3.3.2 Drain Voltage at Saturation

Now, the point of saturation is achieved when channel conductance ($g_c = \frac{\partial I_D}{\partial V_D}$)

becomes zero.

Let,

$$G(I_D, V_D, V_G) = \int_0^L dt(x) \left[(-B + \sqrt{t})^4 - 1 \right]^2 = -4AC\xi_c dx \quad (3.19)$$

Hence,

$$g_c = \frac{\partial I_D}{\partial V_D} = - \frac{\frac{\partial G}{\partial V_D}}{\frac{\partial G}{\partial I_D}} \quad (3.20)$$

$$\frac{\partial G}{\partial V_D} = -4AC \left[(-B + \sqrt{t_L})^4 - 1 \right]^2,$$

$$\frac{\partial G}{\partial I_D} = 4AC \left[R_D \sqrt{P(-B + \sqrt{t_L})^4 - 1} + R_S \sqrt{P(-B + \sqrt{t_0})^4 - 1} \right]$$

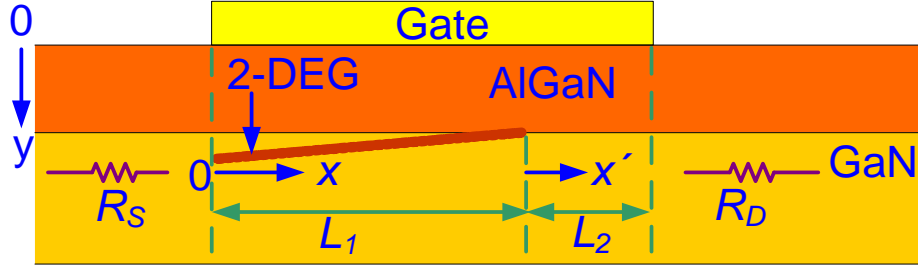


Figure 3.3: Schematic of channel layer for AlGaN/GaN HEMT after saturation

Therefore,

$$g_c = \frac{P(-B + \sqrt{t_L})^4 - 1}{\left[R_D \sqrt{P(-B + \sqrt{t_L})^4 - 1} + R_S \sqrt{P(-B + \sqrt{t_0})^4 - 1} \right]^{1/2}} \quad (3.21)$$

At saturation,

$$P(-B + \sqrt{t_L})^4 - 1 = 0$$

Hence,

$$V_{D,sat} \geq V_G - V_{off} + I_D R_D - k_1 - \frac{B}{C} \sqrt{\frac{I_D}{G_0}} - \frac{A}{C} \frac{I_D}{G_0} \quad (3.22)$$

3.3.3 Drain Current after Saturation

At the onset of saturation, the channel has been divided into regions: low field region, $0 \leq x \leq L_1$, and high field region, $L_1 \leq x \leq L$. Let $x' = x - L_1$. In the high field region two dimensional Laplace's equation is solved to find the current equation.

$$\frac{\partial^2 V}{\partial x'^2} + \frac{\partial^2 V}{\partial y^2} = 0 \quad (3.23)$$

subject to the boundary conditions [30] as follows:

$$\begin{aligned}
V(x', y) &= V_G - \frac{I_D y}{\epsilon_2 Z v_s} \\
\frac{\partial V}{\partial x'}(x', d) &= \xi_0 \\
V(x', 0) &= V_G \\
\frac{\partial V}{\partial y}(x', d) &= -\frac{I_D}{\epsilon_2 Z v_s}
\end{aligned} \tag{3.24}$$

Solving equation (3.23),

$$V(x', y) = \frac{2d\xi_0}{\pi} \sinh \frac{\pi x'}{2d} \sin \frac{\pi y}{2d} + V_G$$

The voltage across the high-field region,

$$V_L - V_{L_1} = \frac{2d\xi_0}{\pi} \sinh \frac{\pi L_2}{2d} \tag{3.25}$$

$V_{L_1} = V_{D,sat}$ and hence equation (3.25) yields after replacing V_{L_1} with equation (3.22),

$$L_2 = \frac{2d}{\pi} \sinh^{-1} \lambda \tag{3.26}$$

where

$$\lambda = \frac{\pi \left(k_1 + V_D - V_G + V_{off} - I_D R_D + \frac{A}{C} \frac{I_D}{G_0} + \frac{B}{C} \sqrt{\frac{I_D}{G_0}} \right)}{2d\xi_0}$$

Now, $L_1 + L_2 = L$ and from equation (3.14),

$$L_1 = -\frac{I_D Y}{4AC\xi_c} \tag{3.27}$$

where

$$Y = \frac{4A^2}{G_0} II_1 + \frac{2AB}{\sqrt{I_D G_0}} II_2$$

and II_1 and II_2 are defined by equation (3.16) and equation (3.17), respectively with $\theta_L = \theta_{L_1} = 0$.

Combining equation (3.26) and equation (3.27) yields the current-voltage characteristics after saturation,

$$I_{D,sat} = I_D = -\frac{4AC\xi_c}{Y} \left(L - \frac{2d}{\pi} \sinh^{-1} \lambda \right) \quad (3.28)$$

where $\xi_0 = p\xi_c$, p is the fitting parameter for smooth transition of drain current from linear to saturation region.

3.4 Small Signal Parameters

3.4.1 Transconductance

Let,

$$F(V_D, V_G, V_D) = L + \frac{I_D Y}{4AC\xi_c} - \frac{2d}{\pi} \sinh^{-1} \lambda \quad (3.29)$$

where,

$$Y = \frac{4A^2}{G_0} I_1 + \frac{2AB}{\sqrt{I_D G_0}} I_2 \quad (3.30)$$

$$I_1 = \int_0^{\theta_{L1}} \sec \theta \tan^2 \theta \cdot d\theta, \quad I_2 = \int_0^{\theta_{L1}} \sqrt{\sec \theta} \tan^2 \theta \cdot d\theta$$

At saturation, $\theta_{L1} = 0$

$$g_m = \frac{\partial I_D}{\partial V_G} = -\frac{\frac{\partial F}{\partial V_G}}{\frac{\partial F}{\partial I_D}} \quad (3.31)$$

$$\frac{\partial F}{\partial V_G} = \frac{I_D}{4AC\xi_c} \frac{\partial Y}{\partial V_G} - \frac{2d}{\pi} \frac{\partial}{\partial V_G} \left(\sinh^{-1} \lambda \right) \quad (3.32)$$

$$= \frac{-\sqrt{P(-B + \sqrt{t_0})^4 - 1}}{\xi_c} + \frac{1}{\xi_0 \sqrt{\lambda^2 + 1}}$$

$$\frac{\partial F}{\partial I_D} = \frac{A}{CG_0 \xi_c} \int_0^0 \sec \theta \tan^2 \theta \cdot d\theta + \frac{B}{4C\sqrt{I_D G_0} \xi_c} \int_0^0 \sqrt{\sec \theta} \tan^2 \theta \cdot d\theta$$

$$- \frac{1}{4ACI_D \xi_c} \sqrt{P(-B + \sqrt{t_0})^4 - 1} \left(\sqrt{t_0} - t_0 + 4ACR_s I_D \right) \quad (3.33)$$

$$- \frac{1}{\xi_0 \sqrt{\lambda^2 + 1}} \left(\frac{A}{CG_0} + \frac{B}{2C\sqrt{G_0 I_D}} - R_D \right)$$

Using equation (3.32) and equation (3.33) in equation (3.31), transconductance after drain current saturation can be calculated.

3.4.2 Cutoff Frequency

Channel charge in the saturation region can be written as,

$$Q = qZ \int_0^{L_1} n_s dx + qZ \int_{L_1}^L n_s dx \quad (3.34)$$

In the region $L_1 < x < L$,

$$n_s = \frac{I_D}{qZv_s}$$

Hence from equation (3.20),

$$Q = qZ \int_0^{L_1} n_s dx + \frac{I_D L_2}{v_s} \quad (3.35)$$

Then using equation (3.9),

$$\int_0^{L_1} n_s dx = \int_0^{L_1} \frac{R^2}{4A^2 \xi_c} \sqrt{\frac{1}{16A^4} \left(\frac{G_0}{I_D} \right)^2 R^4 - 1} \quad (3.36)$$

Performing variable transformation on equation (3.22),

$$Q = \frac{-qZB}{16A^3 C \xi_c P^{3/4}} \int_0^{\theta} \sec^{3/2} \theta \tan^2 \theta \cdot d\theta - \frac{-qZ}{16A^3 C \xi_c P} \int_0^{\theta} \sec^2 \theta \tan^2 \theta \cdot d\theta + \frac{I_D L_2}{v_s} \quad (3.37)$$

where θ and θ_0 are defined by equations (3.12) and (3.15).

Taking derivative of Q with respect to V_G ,

$$C_G = \frac{\partial Q}{\partial V_G} = \frac{-3qZB \sqrt{I_D} g_m}{4C \xi_c \sqrt{G_0^3}} \int_0^{\theta} \sec^{3/2} \theta \tan^2 \theta \cdot d\theta + \frac{qZ}{4A^2 \xi_c} \sqrt{P(-B + \sqrt{t_0})^4 - 1} \quad (3.38)$$

$$- \frac{2qZA g_m I_D}{C \xi_c G_0^2} \int_0^{\theta} \sec^2 \theta \tan^2 \theta \cdot d\theta + \frac{2g_m I_D Y}{4AC \xi_c v_s} - \frac{I_D}{v_s \xi_c} \sqrt{P(-B + \sqrt{t_0})^4 - 1}$$

where Y is defined by equation (3.22).

Unity gain cutoff frequency is given by,

$$f_T = \frac{g_m}{2\pi C_G} \quad (3.39)$$

3.5 Self-Heating Effect

The self-heating is a local increase of crystal temperature due to dissipated Joule electric power [55]. AlGaIn/GaN HEMT exhibits self-heating with the increase in channel power.

The increase in channel temperature is determined by the product of dissipated power and thermal impedance of the device. The equivalent thermal circuit [40] for self-heating effect is shown in Figure 3.4 .

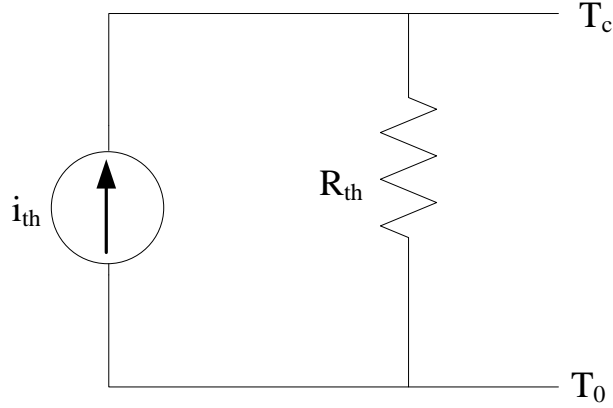


Figure 3.4: Equivalent thermal circuit for self-heating effect

Hence, the channel temperature can be calculated as,

$$\begin{aligned} T_c &= T_0 + i_{th} R_{th} \\ &= T_0 + I_D V_{Di} R_{th} \end{aligned} \quad (3.40)$$

where T_c is the channel temperature, T_0 is the reference temperature, i_{th} is the dissipated power, R_{th} is the thermal impedance of the device. i_{th} is the product of channel current I_D and voltage drop, V_{Di} across the gated part of the channel.

3.5.1 Calculation of Thermal Impedance

Thermal impedance has been calculated using the following expression [57], [58],

$$R_{TH} ZK = \frac{n}{\pi \left[\frac{2 \left(\frac{1}{M} - 1 \right)}{\ln M} - \frac{n-2}{\ln P} \right]} \quad (3.41)$$

Here,

$$M = \frac{2\sqrt{u} + 1}{\sqrt{u} - 1}, \quad u = \frac{\cosh \left[\frac{\pi}{4} \left(\frac{S+L}{F} \right) \right]}{\cosh \left[\frac{\pi}{4} \left(\frac{S-L}{F} \right) \right]}, \quad P = 2 \sqrt{\frac{\cosh \left(\frac{\pi L}{4F} \right) + 1}{\cosh \left(\frac{\pi L}{4F} \right) - 1}}$$

n = Number of gate fingers

Z = Total gate width

L = Gate length

F = Thickness of the layer

S = Spacing between heating elements for multi-finger FET

K = Thermal conductivity of the layer

The thermal conductivity of GaN, SiC or Sapphire decreases with the increase in temperature. The actual temperature would be different from T_c as shown by equation (3.40). Considering temperature dependent thermal conductivity, the actual temperature of the layer can be obtained as follows [58]:

$$T_A \text{ GaN} = \left\{ \frac{T_c - T_0 \left[1 - 0.5 \left(\frac{T_c - T_0}{T_0} \right)^{0.4} \right]}{T_0} \right\}^{-2.5} \quad (3.42)$$

To calculate thermal impedance using equation (3.41), the thermal conductivity at 300 K has been used for GaN. The theoretical limit for intrinsic thermal conductivity due to crystal anharmonicity in wurtzite GaN is 3.36 – 5.40 W/cm.K. In practice, thermal conductivity is a function of doping density and concentration of defects. Researchers [59] have measured the values of thermal conductivity for GaN as low as 1.77 W/cm.K to 0.86 W/cm.K.

Figure 3.6 shows the temperature profile of a field-effect transistor where $T_1 > T_2 > T_3$. The elliptic nature of temperature contours is evident [55], [58]. Hence, the thermal impedance has been calculated considering the gate of the HEMT as the heating element

as shown in Figure 3.5. The dissipated power, i_{th} across the element has been obtained using the following expression:

$$i_{th} = I_D V_D - I_D^2 (R_S + R_D) \quad (3.43)$$

Using equations (3.40) and (3.42), actual channel temperature, T_A has been obtained.

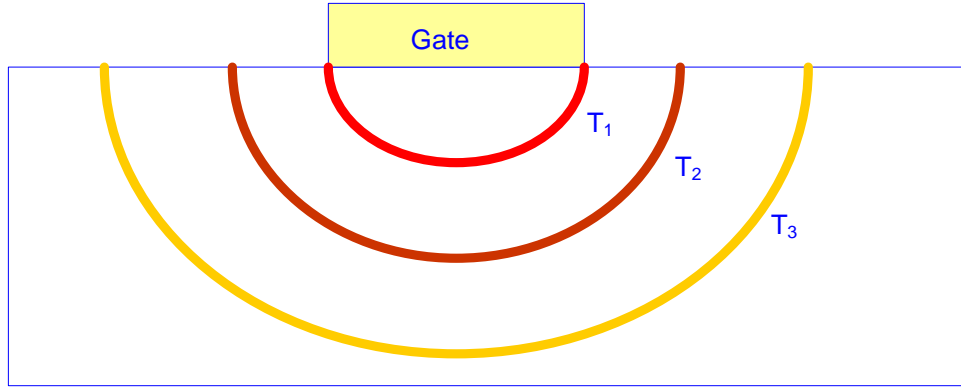


Figure 3.6: Temperature profile of a FET

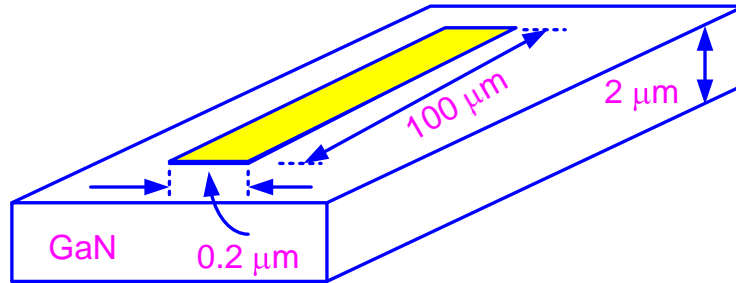


Figure 3.5: Schematic of an equivalent heat source for the calculation of thermal Impedance

3.6 Measurement and Simulation Results

The current-voltage characteristics of the HEMT (Figure 3.1: Sc) have been obtained using Keithley 2400 source meters and Signatone DC probe station. A Labview program has been used to sweep the voltages and measure the currents by the source meters. The transfer characteristics of drain current versus gate-to-source voltage have been obtained using equation (3.28) keeping drain-to-source voltage constant. Figure 3.7 shows the simulated (solid) and the measured (circle) transfer characteristics for $V_{DS} = 10$ V. The analytical curve shows good agreement with the measured data. The threshold voltage is -4.6 V. Figure 3.8 shows the analytical (solid) and the measured (circle) output characteristics of drain current versus drain-to-source voltage for the gate voltages of 0 V to -3 V. The analytical curve has been obtained using equations (3.14) and (3.28) for linear and saturation regions, respectively. The delayed transition between the linear and the saturation regions of the analytical curve occurs due to the carrier velocity saturation in the drift region between the drain and the gate and is equivalent to an increase in the resistance of the drift region [60]. In the model, a constant value of the resistance has been considered and hence, the drain current has been overestimated during the transition. Figure 3.9 shows the simulated output characteristics for higher drain-to-source voltages of up to 50 V. The output conductance becomes negative due to self-heating at the large level of signal.

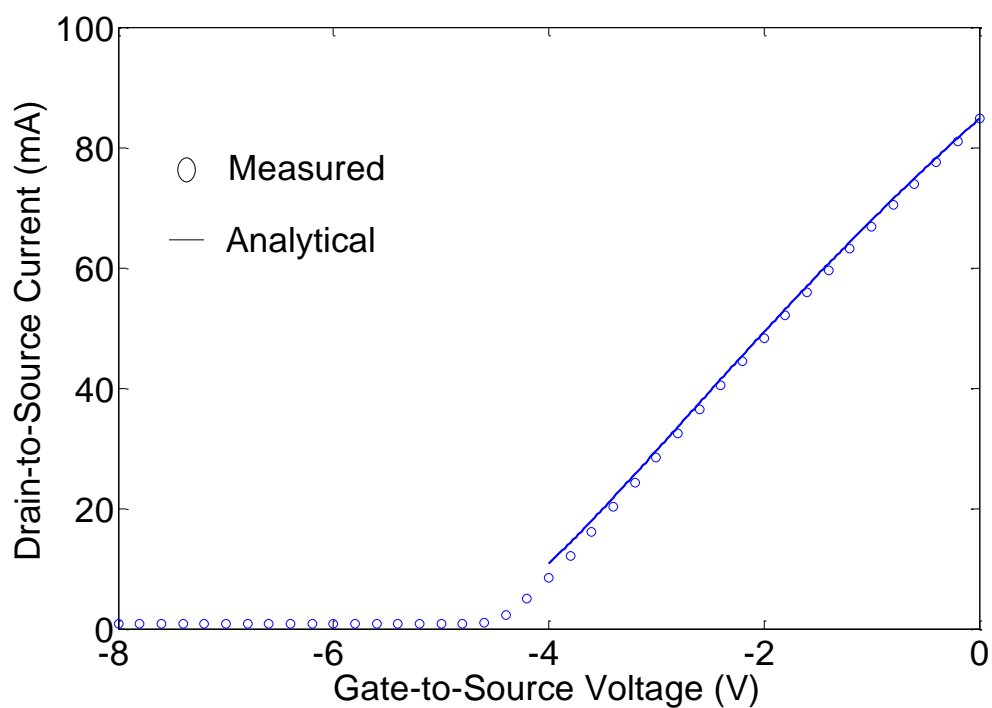


Figure 3.7: Transfer characteristics of AlGaIn/GaN HEMT after saturation ($V_{DS} = 10$ V)

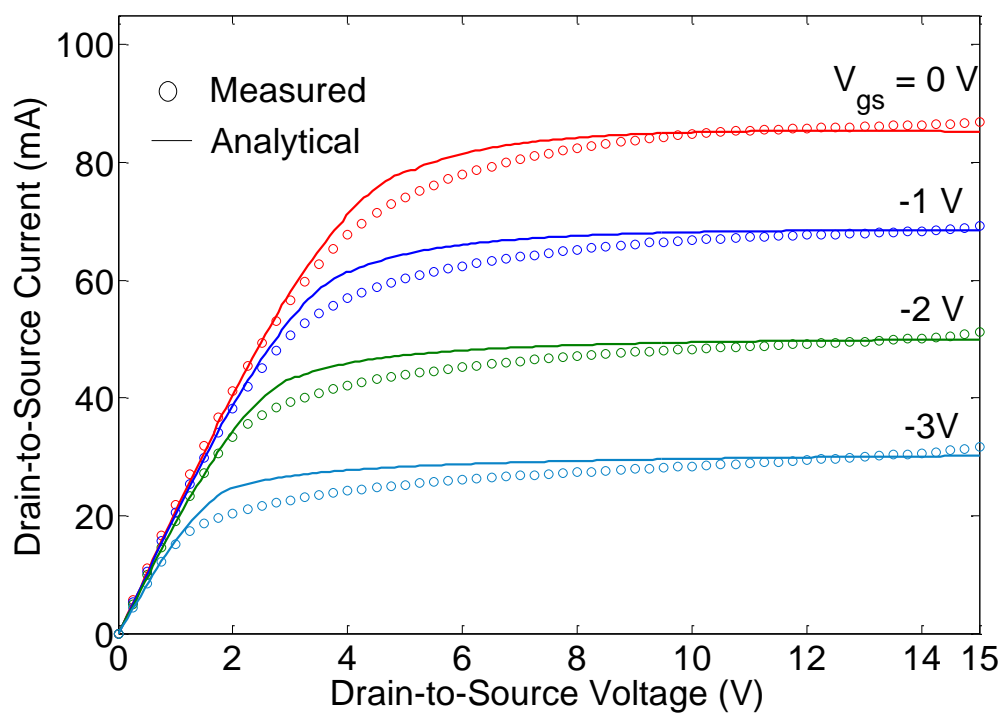


Figure 3.8: Simulated and Measured output characteristics of AlGaIn/GaN HEMT

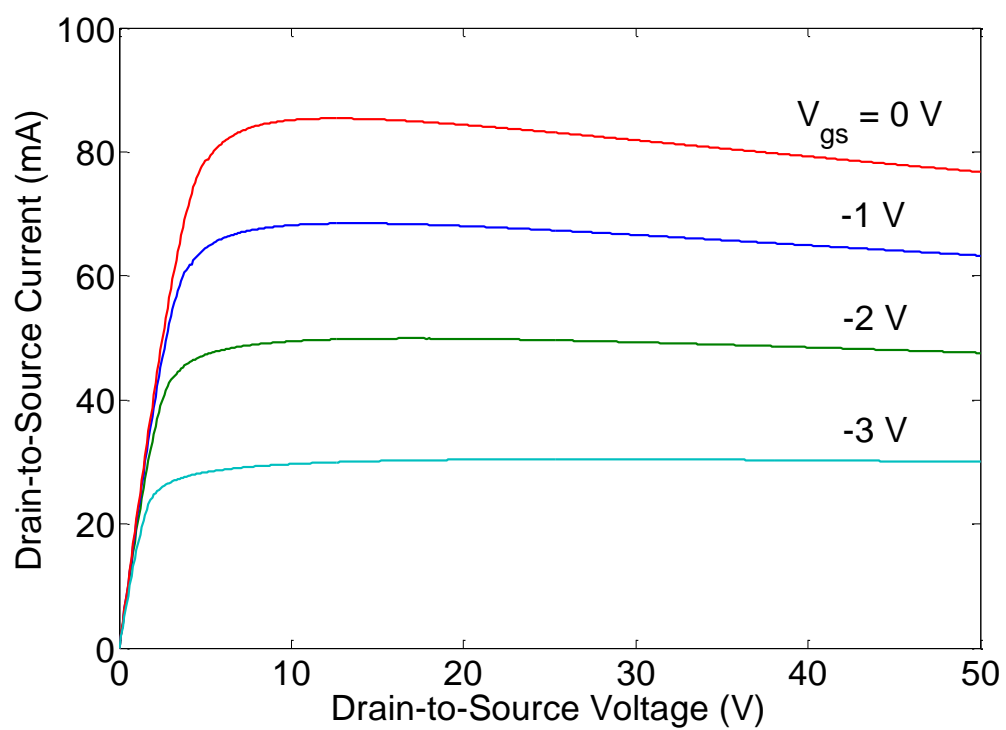


Figure 3.9: Simulated negative output conductance in saturation region when higher drain-to-source voltages are applied

Chapter 4 Temperature Dependent Model

4.1 Introduction

This chapter describes the temperature dependent physics based model to predict the current voltage characteristics, small and large signal parameters of AlGaIn/GaN HEMT for different temperatures. To include the effects of temperature, the temperature dependent parameters of the device have been identified. These are primarily low-field electron mobility, Fermi energy, conduction band offset, effective width of 2-DEG, and thermal conductivity. The variations of these parameters with temperature have been incorporated in the physics based model developed in chapter 3. Temperature- and bias-dependent on-wafer I-V measurements from 300 K to 573 K have been done to validate the model.

4.2 Temperature Dependent Parameters

4.2.1 Fermi Energy

Fermi energy in GaN varies with the sheet charge density, n_s [24] and temperature and is defined [33] by the following polynomial equation,

$$E_F = k_1 + k_2 n_s^{1/2} + k_3 n_s \quad (4.1)$$

where k_1 , k_2 , k_3 are temperature dependent parameters which are obtained from three different values of n_s 's and corresponding E_F 's [33]. Table 4.1 shows the values of k_1 , k_2 , k_3 for three different temperatures as calculated by the method described in [33].

Table 4.1: Values of k_1, k_2 , and k_3 at different temperatures

Temperature (K)	k_1 (V)	$k_2 \times 10^{-7}$ (V.cm)	$k_3 \times 10^{-14}$ (V.cm ²)
300	-0.1526	3.4622	-5.4733
400	-0.2122	4.3243	-9.0229
500	-.2739	5.1828	-12.536

4.2.2 Energy band offset

An important parameter that determines the two-dimensional electron gas density in the HEMT is the conduction band discontinuity ΔE_C at the heterointerface. Higher ΔE_C is expected to produce higher 2-DEG density. In $\text{Al}_m\text{Ga}_{1-m}\text{N}/\text{GaN}$ HEMT, ΔE_C is expressed as [62],

$$\Delta E_C(T, m) = 0.75 \left(E_g^{\text{AlGaN}}(T, m) - E_g^{\text{GaN}}(T, m) \right) \quad (4.2)$$

where m is the Al mole fraction in AlGa_N, T is the lattice temperature and E_g is band gap energy.

The band gap of the alloy $\text{Al}_m\text{Ga}_{1-m}\text{N}$ has been approximated by the quadratic relation

$$E_g^{\text{AlGaN}}(T, m) = m E_g^{\text{AlN}}(T) + (1-m) E_g^{\text{GaN}}(T) - m(1-m) \quad (4.3)$$

The empirical Varshni formula [63] well approximates the temperature dependence of the band gap energy. The band gap energy for AlN and GaN is given by [64], [65],

$$E_g^{AlN} = 6.34 - 1.799 \times 10^{-3} \times \frac{T^2}{T + 1462} \quad (4.4)$$

$$E_g^{GaN} = 3.582 - 9.09 \times 10^{-4} \times \frac{T^2}{T + 830} \quad (4.5)$$

4.3 Quantum Correction

Schrodinger and Poisson equations have been solved self consistently to calculate the average distance of the 2-DEG from the AlGaN/GaN interface [66]. The variation in the average distance of the 2-DEG at different temperatures is shown in Figure 4.1.

4.3.1 Spontaneous and Piezoelectric Polarization

In AlGaN/GaN based heterostructures, large spontaneous and piezoelectric polarization fields exist due to the material properties of AlGaN/GaN [[62], [67]]. Because of this property 2-DEG is formed with very high sheet carrier concentrations of 10^{13} cm^{-2} , even without any intentional doping [68]. Although the spontaneous polarization is very strong in group III nitrides, the pyroelectric coefficients, describing the change of the spontaneous polarization with temperature, are measured to be very small [69], [70]. It has been demonstrated [47] that the effect of pyroelectric coefficients on the channel current at high temperature is negligible.

The piezoelectric polarization P_{pz} in the direction of z-axis can be determined by the elastic and piezoelectric constants [14]. P_{pz} is also found to be nonlinear in terms of the

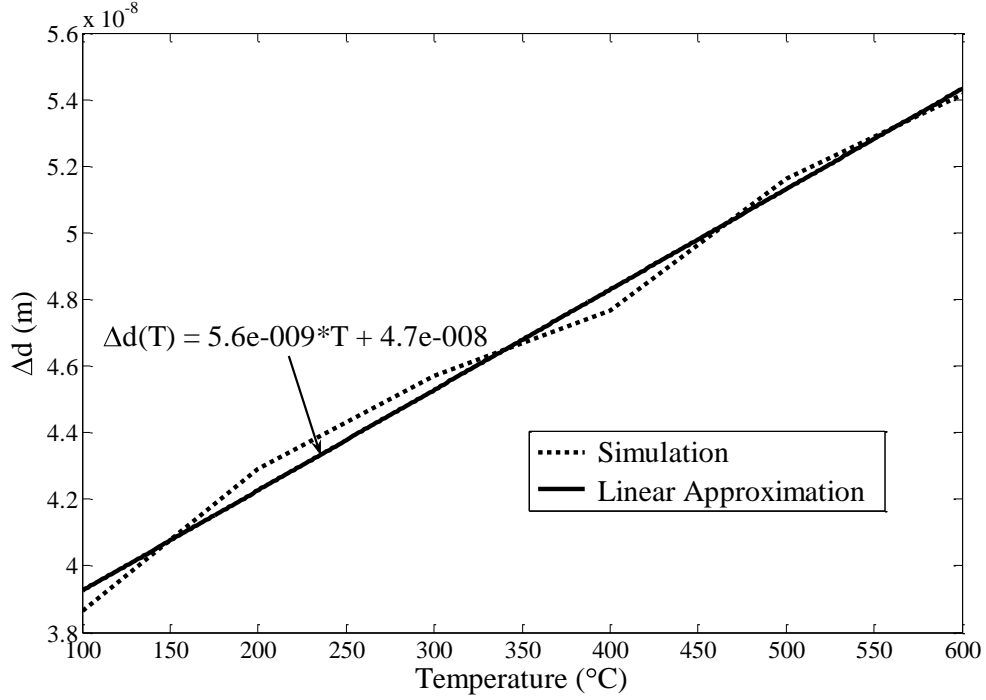


Figure 4.1: Quantum correction (Δd) dependency on temperature

alloy composition. An extensive literature search did not yield any report on the temperature dependence of piezoelectric polarization. Since it is expected to be very

small as in spontaneous polarization, the temperature dependence of piezoelectric polarization is neglected in this model.

4.3.2 Mobility

Mobility is identified as the key parameter in the physics based model for significantly altering the transistor characteristics with variations of temperature. Authors in [71] presented a simple analytical model to describe the temperature and concentration

dependencies of the low-field mobility in bulk doped GaN material. In the paper [71], the low –field mobility in terms of temperature is expressed as,

$$\mu_0(N, T) = \mu_{\max} \frac{B(N) \left(\frac{T}{T_0}\right)^\beta}{1 + B(N) \left(\frac{T}{T_0}\right)^{\alpha+\beta}} \quad (4.6)$$

Where α and β are constants with values 0.7 and 0.2 respectively for electrons and $B(N)$ is defined as follows in [71],

$$B(N) = \left[\frac{\mu_{\min} + \mu_{\max} \left(\frac{N_g}{N}\right)^\gamma}{\mu_{\max} - \mu_{\min}} \right] \quad (4.7)$$

Model parameters μ_{\min} , μ_{\max} , N_g , and γ are dependent on semiconductor material and N is the doping concentration of the semiconductor. The 2-DEG mobility is function of the 2-DEG density, n_s which in turn is function of gate-to-source voltage. Hence, in this paper the low-field mobility is defined by a phenomenological model [72],

$$\mu_0 = \frac{p_1}{p_2 + p_3 + V_{gs}^2} \quad (4.8)$$

where p_1 , p_2 and p_3 are extracted parameters. The empirical relation between 2-DEG mobility and temperature incorporated in the presented model is as follows [73],

$$\mu_T = \mu_{300K} \left(\frac{T}{300}\right)^{-1.8} \quad (4.9)$$

4.4 Simulation and experimental results

By incorporating the temperature variation of the model parameters in equations (3.14) and (3.28), the output characteristics between drain-to-source current and drain-to-source

voltage are obtained at different temperatures as shown in Figure 4.3 for gate-to-source voltage of 0V. The analytical curve matches very closely with the measured data as shown for three different temperatures (Figure 4.3). The bulk resistances from gate-to-source and gate-to-drain are assumed to be constant in this formulation of the analytical model. These resistances are function of 2-DEG density and carrier mobility across the non-gated regions. Due to larger spacing between the gate and the drain terminals of this power device the drain resistance becomes larger than the source resistance. By including the variation of bulk resistances and Schottky barrier height [73], [74] with temperature, the current-voltage characteristics can be more accurately predicted.

Figure 4.2 shows the variation of transconductance with gate-to-source voltage for different temperatures. The transconductance plot (Figure 4.2) has been obtained by considering temperature variation of the parameters and applying equation (3.31). Similarly, unity gain cutoff frequency with varying temperatures (Figure 0.1) has been calculated using the temperature dependent expressions of the parameters and applying equation (3.39).

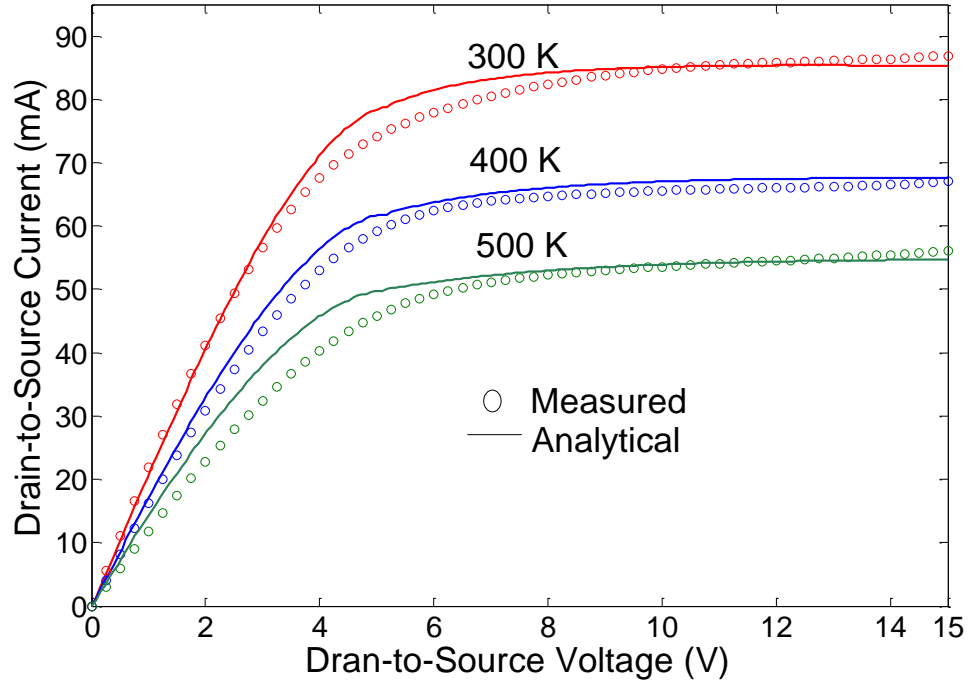


Figure 4.3: Analytical and Measured output characteristics of AlGaIn/GaN HEMT at $V_{GS} = 0$ V for varying temperature

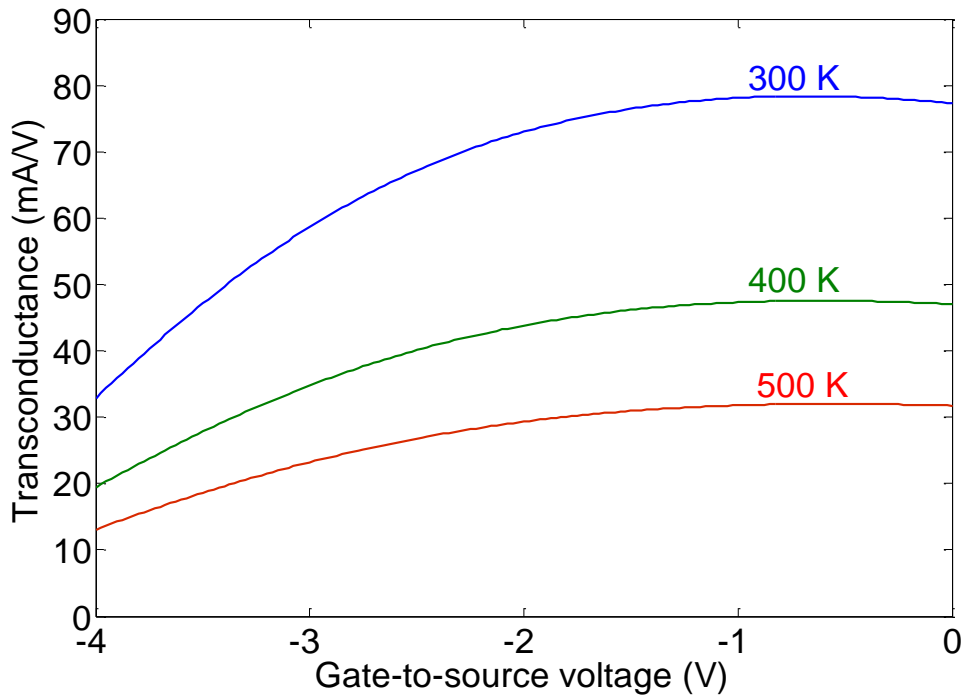


Figure 4.2: Simulated transconductance of the HEMT with variation of gate-to-source voltage and V_{DS} of 10 V for varying temperature

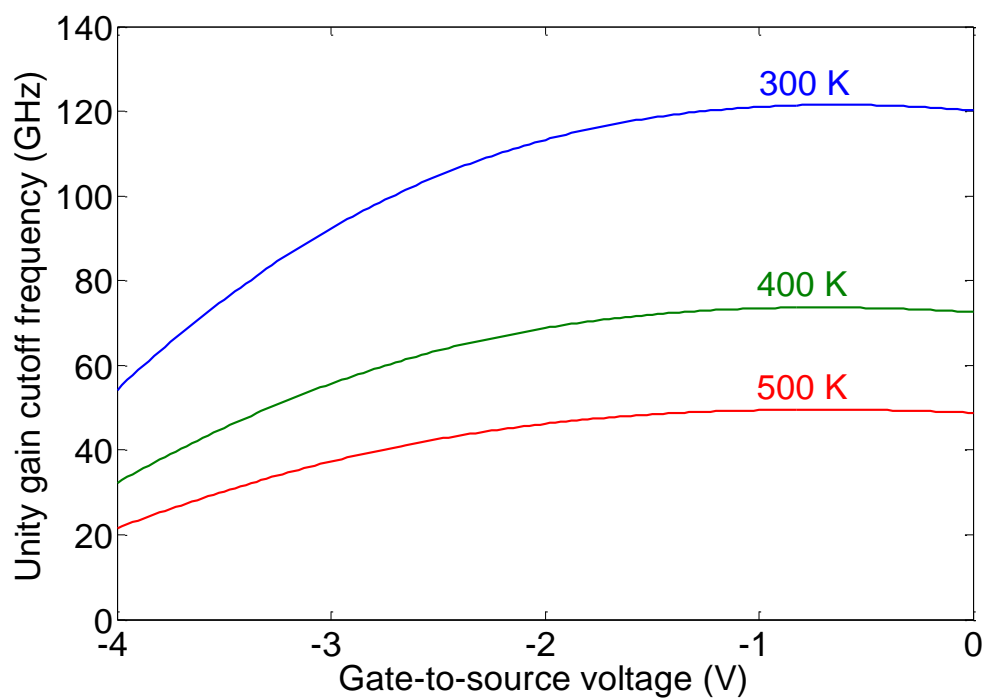


Figure 0.1: Simulated unity gain cutoff frequency of the HEMT with variation of gate-to-source voltage and V_{DS} of 10 V for varying temperature

Chapter 5 AlGaIn/GaN HEMT as Sensor

5.1 Introduction

This chapter describes the application of the physics based model of AlGaIn/GaN HEMT to CHEMFET/sensor. AlGaIn/GaN HEMT based CHEMFET technique has been applied for the detection and the characterization of biomolecular photovoltaic PS I reaction centers. In oxygenic plants, photons are absorbed with high quantum efficiency by two specialized reaction centers, Photosystem I (PS I) and Photosystem II (PS II). PS I reaction centers have been extracted, purified and anchored on a metal surface without denaturation. PS I reaction centers can be self-assembled and oriented on organosulfur-modified gold substrates. Absorption of photon triggers rapid charge separation and the conversion of light energy into an electric potential across the nanometer-scale (~6 nm) dimension of reaction centers. Investigating the physics of the AlGaIn/GaN HEMT and the floating gate field-effect transistor, an analytical model has been developed to estimate the number of PS I reaction centers effectively oriented on the floating gate surface of an AlGaIn/GaN HEMT. This work effectively demonstrates a practical approach for the electrical characterization of PS I reaction centers to date as other methods of characterization are primarily heavy laboratory instrument oriented.

In this chapter, the significance of PS I reaction centers as unlimited source of solar energy has been described first. Then AlGaIn/GaN HEMT based CHEMFET technique

for the characterization of PS I reaction centers has been discussed, and finally the analytical model for the CHEMFET has been elaborated.

5.2 Role of Photosystem I Reaction Centers

PS I reaction centers are potential sources of solar energy. Using sunlight, these reaction centers generate electrical potentials which can be accumulated to build substantial source of electrical energy if proper extraction technique can be developed. In oxygenic plants there are two types of reaction centers – Photosystem I (PS I) and Photosystem II (PS II). Both of the reaction centers work in succession to produce glucose for green plants, some bacteria and protistans in photosynthesis. Photosynthesis is a two phase process. The first phase is light dependent which requires direct energy of light to produce energy carrier molecules. The second phase is light independent. During the first phase, light energy induces electron separation in PS II. PS II fills the electron from a water molecule, breaking the water into H^+ ions and O^{2-} ions. These O^{2-} ions combine to form O_2 molecule. The electron is boosted to a higher energy state and finally transferred to PS I through electron acceptor and a series of redox (reduction + oxidation) reactions. The electron is again passed through a series of redox reactions and eventually becomes attached to $NADP^+$ and H^+ to form NADPH, which is energy carrier in the light independent reaction. There is thus a continuous flow of electrons from water to NADPH, which is used for carbon fixation in the light independent process. Thus, PS I and PS II work as energy harvesting units in photosynthesis. Figure 5.1 shows the schematic for the entire chain of photosynthesis.

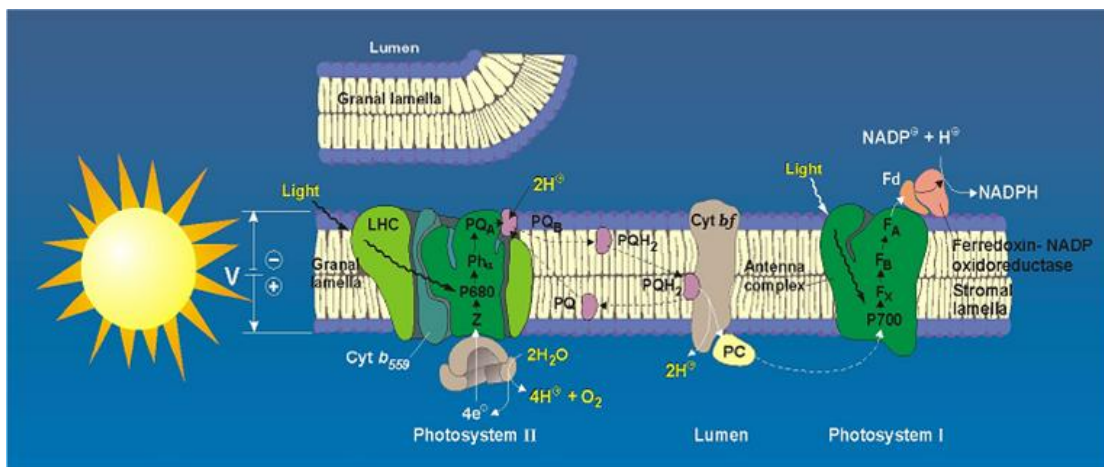


Figure 5.1: Role of reaction centers in photosynthesis (used with permission from Dr. Lee)

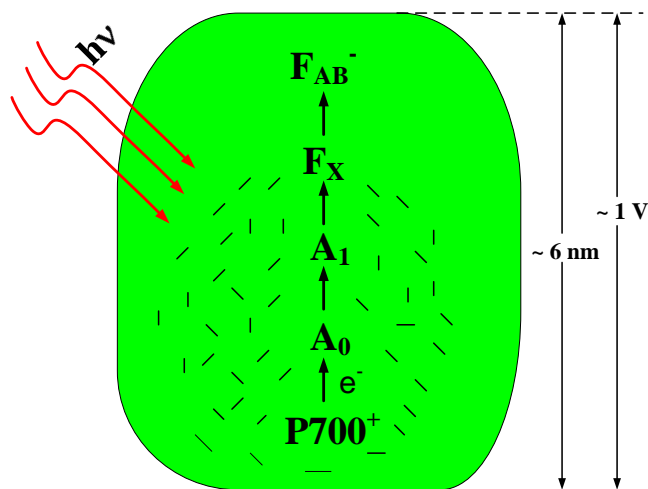


Figure 5.2: Schematic illustration of the structure and function of an isolated PS I reaction center core antenna complex

5.2.1 Structure of Photosystem I Reaction Center

PS I reaction center can be isolated efficiently from thylakoids of plant leaves (such as spinach) using the technique of detergent solubilization and hydroxylapatite column purification [82]. Each reaction center contains about 40 chlorophylls per photoactive reaction center (P700 in Figure 5.2). The isolated PS I complexes are elliptical in shape with major and minor axes of about 6 and 5 nm, respectively [82].

Figure 5.2 shows the approximate structure and pigments of PS I reaction centers. An isolated PS I complex contains electron acceptors (A_0 , A_1 , F_X and F_{AB}) in addition to P700 and the antenna chlorophylls. Chlorophylls serve as an antenna to capture photons and transfer photon energy to P700. The photochemistry of P700 generates a primary charge separation ($P700^+ A_0^-$) within about 1.5 pico second [83]. Due to efficient excitation transfer and trapping, the entire photophysical chemistry can be completed in 10-30 pico seconds. The electron released from P700 is transferred to the terminal acceptor F_{AB} at the reducing side of PS I, through intermediate acceptors A_0 , A_1 and F_X . The quantum yield of PS I photochemistry is very close to 100%. Charge separation in this natural photovoltaic device generates a potential difference of about 1 volt across about 6 nm between the reduced (F_{AB}^-) and oxidized ($P700^+$) sides of the PS I complex, resulting in a very strong electric field ($\sim -10^8$ volts per meter). The first measurement of exogenous photovoltages generated from single PS I reaction centers immobilized on atomically flat gold surfaces has been done using the technique of Kelvin force probe microscopy (KFM) [84]. However, no two-terminal micro device or sensor has been

developed for the characterization of these biomolecular photodiodes. AlGaIn/GaN HEMT based CHEMFET is a convenient technique for the characterization of PS I reaction centers.

5.3 Immobilization of PS I Reaction Center

Organic self-assembled monolayers (SAMs) on solid surfaces have been regarded as one of the most suitable functional linkage-layers for the immobilization of biomolecules. To date, the most intensively studied systems are SAMs of alkanethiols on gold surfaces. Functional PS I reaction centers can be selectively immobilized and oriented by chemical modification of a surface [82]. Two-dimensional vectorial arrays of functional PS I reaction centers have been prepared on atomically flat derivatized gold surfaces [82]. The atomically flat Au {111} substrate treated with mercaptoacetic acid (HSCH_2COOH), 2-dimethylaminoethanethiol [$(\text{CH}_3)_2\text{NCH}_2\text{CH}_2\text{SH}$], or 2-mercaptoethanol ($\text{HSCH}_2\text{CH}_2\text{OH}$) can form a negative, positive, or hydrophilic surface, respectively. After incubating the substrates in PS I solution, it has been found that 65% of the area was covered with PS I when the gold electrode was treated with mercaptoacetic acid with negatively charged end groups that attract and orient PS I reaction centers. Previous studies have shown that the polar regions (both ends) of the PS I are positively charged [82]. These regions serve as the docking sites for ferredoxin and plastocyanin, the natural electron acceptor and donor, respectively, for PS I. On the other hand, very little PS I coverage was found (i.e., 5.0%), on 2-dimethylaminoethanethiol—treated gold surface terminated with positively charged end groups [82]. Hence, a positively charged surface does not attract PS I very

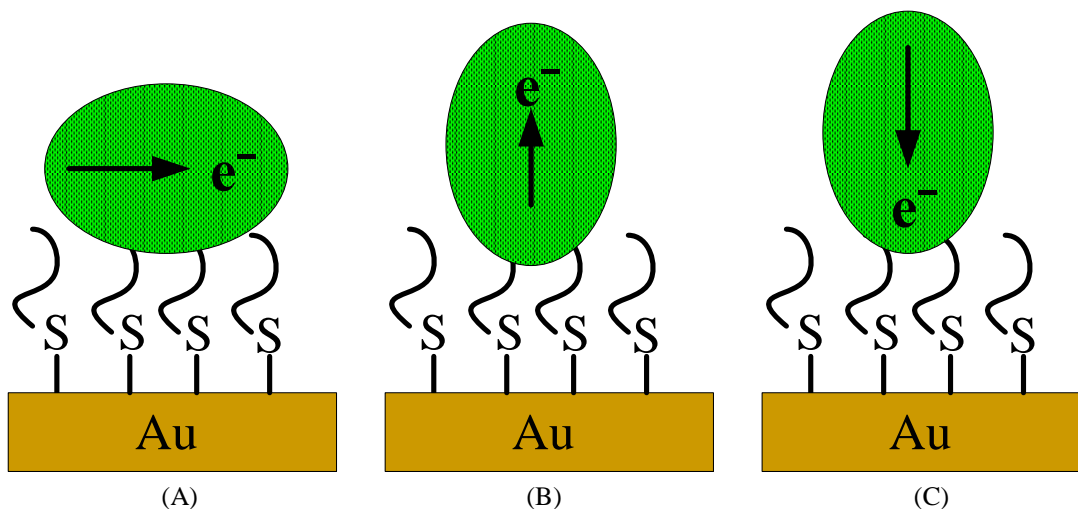


Figure 5.3: The orientation of individual PSI reaction center

well. When the gold electrode was treated with 2-mercaptoethanol, 70% of the area was covered with PS I. This chemical treatment terminates the surface with end groups that form hydrogen bonds with PS I and can also be used to construct arrays of PS I reaction centers on gold surfaces.

In addition, the orientation of PS I can be selectively made by chemical modification of a surface. For mercaptoacetic acid, 83% of the electron transport vectors were parallel to the surface Figure 5.3A, whereas with 2-mercaptoethanol 70% were oriented perpendicularly in the “up” position (with P700 facing the Au surface) (Figure 5.3B) and only 2% were in the “down” position (Figure 5.3C). No preferential orientation was observed with 2-dimethylaminoethanethiol.

5.4 AlGaN/GaN CHEMFET

The concept of AlGaN/GaN HEMT based CHEMFET for the characterization of reaction centers is illustrated in Figure 5.4. PS I reaction centers are immobilized on the chemically modified gate (Au) surface of the HEMT. Upon illumination, PS I reaction centers create positive charges on the surface and eventually modulate the 2-DEG at the hetero interface. This results in an increase in drain current of the CHEMFET.

5.4.1 Experiment and Results

Before immobilization of the reaction centers on the AlGaN/GaN HEMT, the characteristics of the bare HEMT have been measured in dark and light environments.

The photochemical activity (Figure 5.5) and light absorption characteristics (Figure 5.6) of PS I reaction centers have been measured before immobilization. As shown in Figure 5.5 with the light on, PS I signal rises immediately and remains in the steady state as long

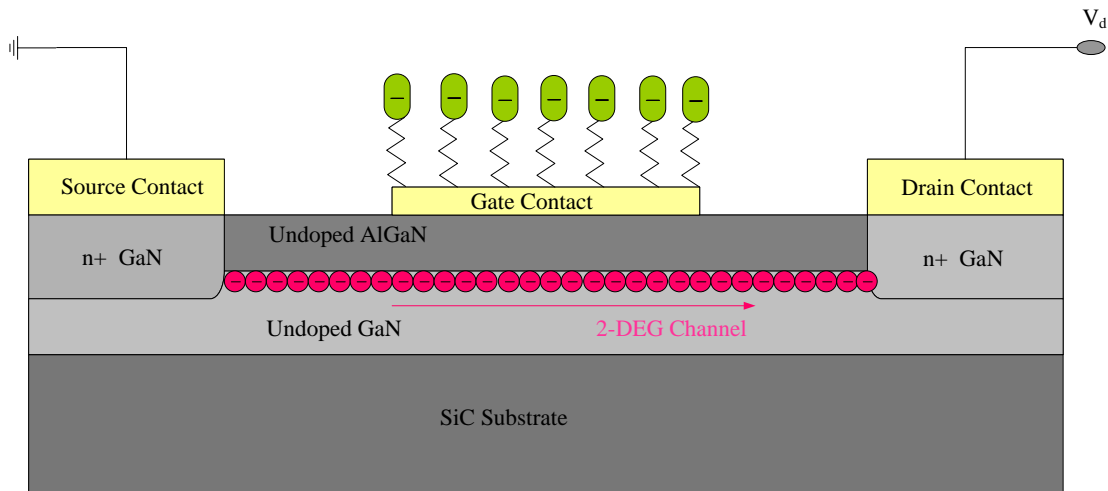


Figure 5.4: PS I Reaction Centers immobilized on the gate of an AlGaN/GaN HEMT

as the light is on. With the turn off of light, the signal of PS I goes down to the previous state. Thus, the photochemical activity of PS I has been confirmed with the measurement shown in Figure 5.5. Figure 5.6 confirms the light absorption performance of chlorophylls as an antenna in the reaction centers. The absorption maximizes at two wavelengths of light such as 437 nm (blue), and 672 nm (red).

The surface of the AlGaIn/GaN HEMT has been treated with 2-mercaptoethanol to functionalize for PS I reaction centers. After waiting for 30 second, the die has been immersed with filtered solution of PS I and kept in refrigerator for 24 hours. The dc current voltage characteristics have been measured by Signatone dc probe station with Keithley source meter for the sweep of drain-to-source voltage. The measurement has been done under floating gate condition in both dark and white light identical to the conditions during bare surface measurement of the HEMT. Figure 5.7 shows the schematic of the HEMT on the die and microphotograph of the die during measurement of current-voltage characteristics under floating gate condition.

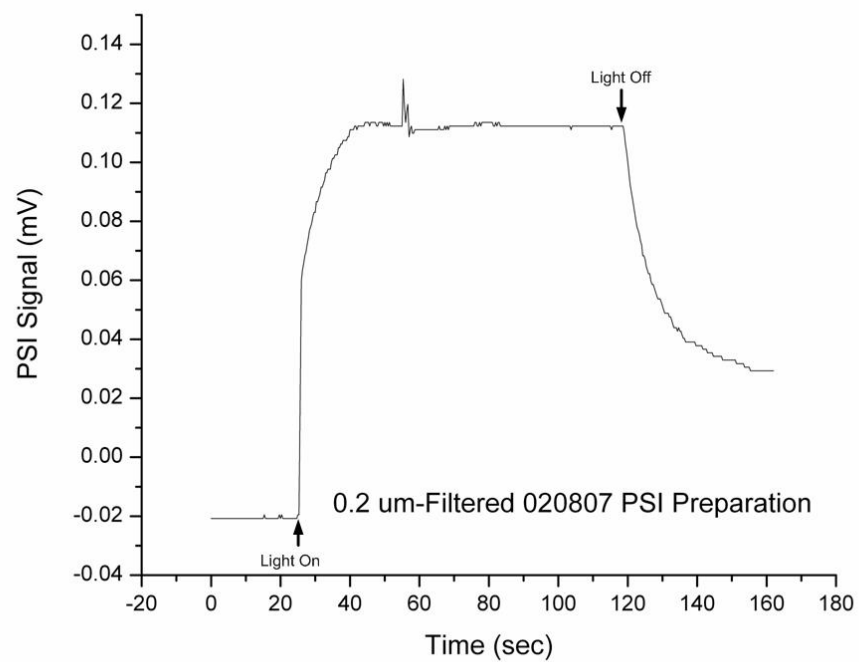


Figure 5.5: Kinetic profile of P700+ steady-state formation and reduction

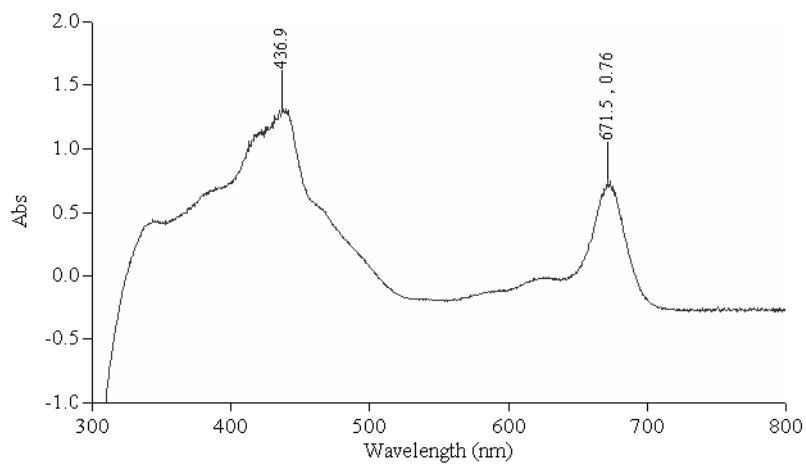


Figure 5.6: Absorption spectrum of PS I reaction centers

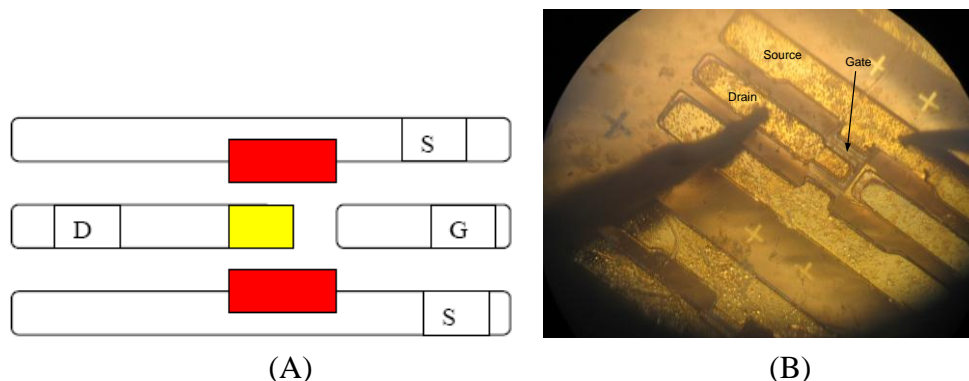


Figure 5.7. (A) Schematic of parallel HEMTs (B) Microphotograph of the HEMT during I-V measurement

Figure 5.8 shows the output characteristics of the HEMT measured up to drain-to-source voltage of 3 V. In this figure the light-dark characteristics of the bare HEMT and the PS I modulated HEMT have been plotted. The light current is less than the dark current for the bare HEMT measurement, which explains photon-assisted charge collapse from the 2-DEG. Figure 5.9 shows change in light and dark characteristics of the HEMT due to immobilization of PS I reaction centers. The change in light current for PS I has been obtained by deducting the light current of the bare HEMT from the total light current of the PS I modulated-HEMT. Similarly, the change in dark current for PS I is found by subtracting the dark current of the bare HEMT from the total dark current of the PS I modulated-HEMT.

As reported in [82], 70-80% of PS Is on 2-mercaptoethanol-modified gold surfaces is oriented primarily with the electron acceptor side up and the P700 donor side down (adjacent to the 2-mercaptoethanol-modified gate surface). Under illumination, the electric potential on the oxidizing side (P700) of PS I develop a positive voltage

following electron release, whereas in the dark, the potential is negative [84]. Thus, under the light, the 2-DEG density is enhanced due to positive charges created by PS I reaction centers at the surface. As a result, the change in drain current due to PS I in light is positive and increases with the increase in drain-to-source voltage as seen from Figure 5.9. On the other hand, in dark, the change in current is negative and increases with the applied voltage. This behavior implies that the negative charges of PS I in dark drive the device toward inversion. Also, the changes in light current are less than the changes in dark current with the applied voltage as shown in Figure 5.9, which implies that not all of the reaction centers immobilized have been activated by light to create effective positive charges on the gate surface.

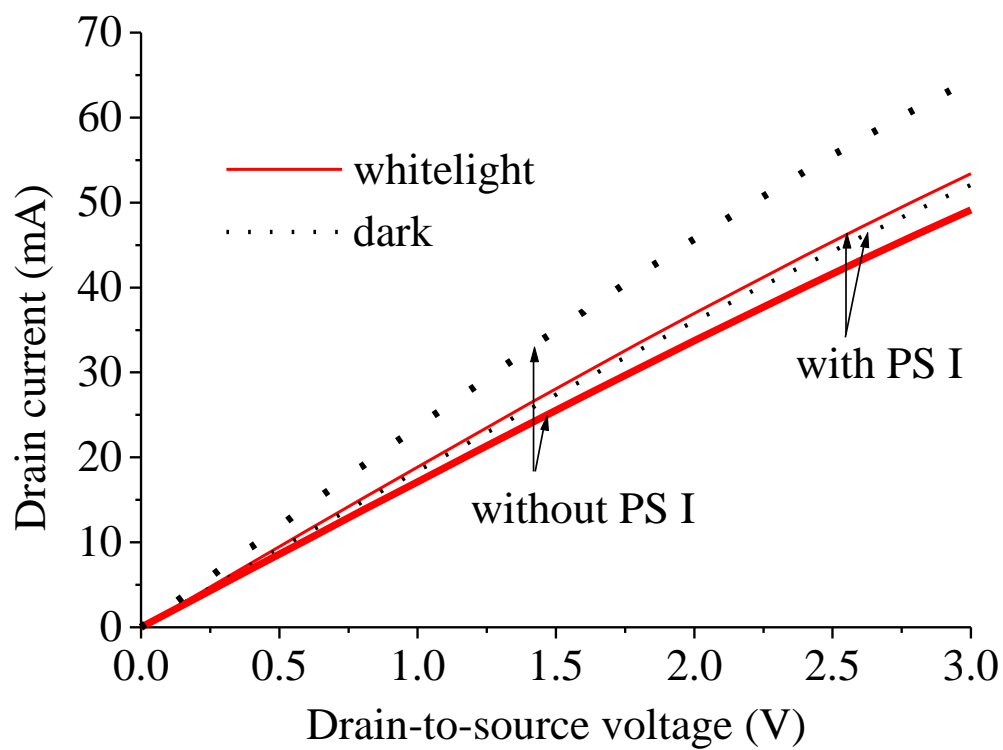


Figure 5.8: Light and dark characteristics of the HEMT ($L = 0.2 \mu\text{m}$, $W = 100\mu\text{m}$) without any external layer and with immobilized PS I reaction centers on the surface. Dotted and solid lines represent dark and light responses, respectively in both cases.

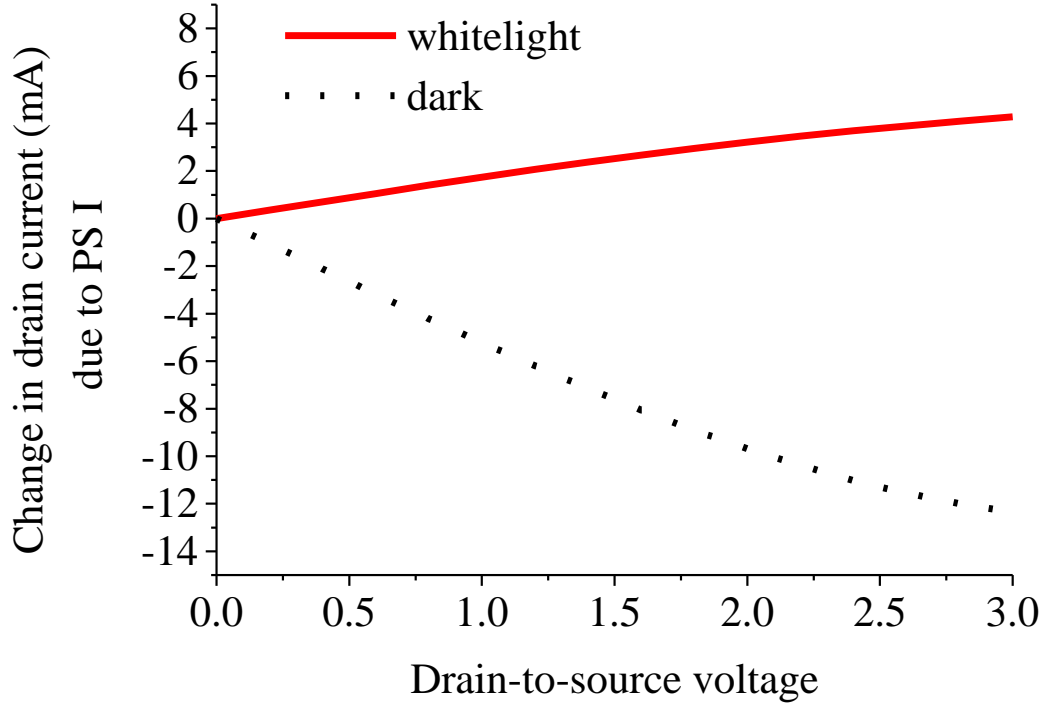


Figure 5.9: Change in light (solid) and dark (dotted) characteristics of the HEMT due to immobilization of PS I reaction centers only

5.5 Model formulation

Let, I_{D1} and I_{D2} represent the drain-to-source currents measured in light for the PS I modulated HEMT and for the bare HEMT, respectively with a drain-to-source voltage applied for linear region of operation.

The drain current of a HEMT can be expressed as,

$$I_D = qn_s \left(\frac{Z_v}{L} \right) \quad (5.1)$$

where $n_s(x)$ is the sheet carrier density, which is defined under floating gate condition by,

$$n_s = \frac{\varepsilon_2}{q(d_d + \Delta d)} (V(x) - V_{th}) \quad (5.2)$$

where ε_2 is permittivity of AlGaIn, d_d is the thickness of AlGaIn layer, Δd is the effective thickness of the 2-DEG channel, $V(x)$ is the voltage at x in the 2-DEG channel due to applied drain bias, V_{th} is the threshold voltage which can be expressed as [[27],[30]],

$$V_{th} = \phi_b - \frac{\Delta E_c}{q} + \frac{\Delta E_{F1}}{q} - \frac{\sigma d_d}{\varepsilon_2} \quad (5.3)$$

where ϕ_b is Schottky-barrier height between gate metal and AlGaIn, ΔE_c is conduction band discontinuity, ΔE_{F1} is the change in Fermi energy at the heterointerface (0 at 300 K), σ is the sheet charge density due to spontaneous and piezoelectric polarizations. Following the approximation described earlier, for each positive or negative ion adsorbed at the free surface of the HEMT, one electron is gained or lost in the 2-DEG. According to the models of floating gate transistor and CHEMFET theory, the binding of PS I charges will be reflected in changes, ΔV_{th} of threshold voltage or floating gate voltage, V_{FG} as follows,

$$V_{FG} = \Delta V_{th} = -\frac{Q}{C_{gc}} = -\frac{Q(d + d_r)}{\varepsilon_2} \quad (5.4)$$

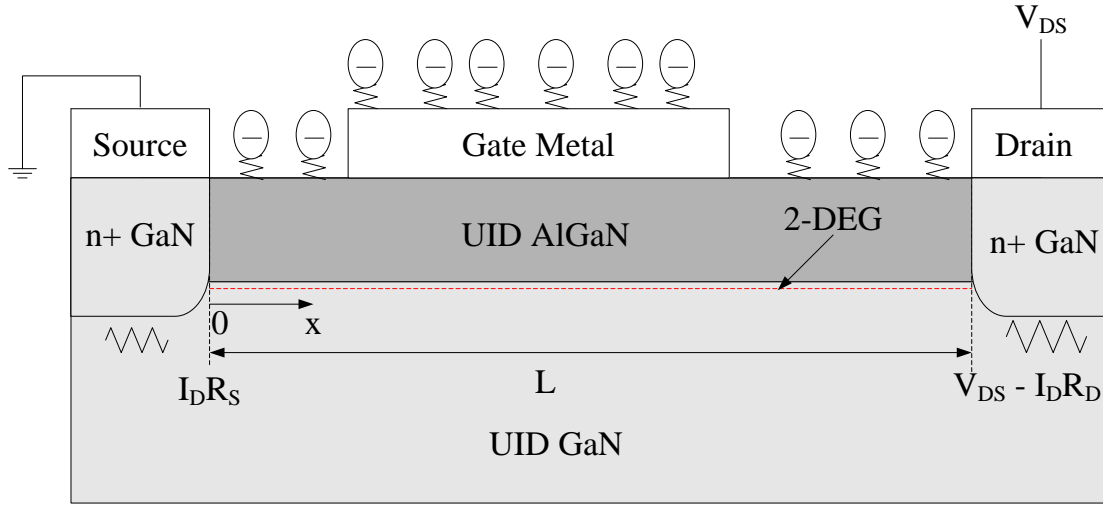


Figure 5.10: Schematic of the AlGaIn/GaN CHEMFET with PS I reaction centers for analytical modeling (drawn not to scale).

where Q is the effective charge per unit area and C_{gc} is the gate-channel capacitance, d is defined by $\Delta d + d_d$, d_r is the root mean square (RMS) roughness (Figure 5.11) of gate surface and $v(x)$ is the drift velocity which is related to the longitudinal electric field $E(x)$ by,

$$v = \frac{v_s E}{\sqrt{E^2 + E_c^2}} \quad (5.5)$$

where v_s is saturation velocity of electron in GaN, $E_c = \frac{v_s}{\mu_0}$, μ_0 is low-field mobility of

electron in the 2-DEG. Now, change in drain current measured under illumination due to presence of PS I reaction centers can be analytically expressed as,

$$\Delta I = I_{d1} - I_{d2} = q \left(n_{s1} - n_{s2} \right) \mu_0 E \quad (5.6)$$

Combining equations (5.2) – (5.6),

$$\begin{aligned}\Delta I &= q \frac{\varepsilon_2}{d} \Delta V_{th} \frac{E v_s}{\sqrt{E^2 + E_c^2}} Z \\ &= -GQ \frac{E}{\sqrt{E^2 + E_c^2}}\end{aligned}\tag{5.7}$$

where $G = \frac{d + d_r}{d} Z v_s$. Equation (5.7) can be written as,

$$E = \frac{E_c}{\left[\left(\frac{GQ}{\Delta I} \right)^2 - 1 \right]^{1/2}}\tag{5.8}$$

Substituting E by $\frac{dV}{dx}$ and integrating from $x = 0$ to $x = L$,

$$Q = \frac{\Delta I}{G} \left[1 + \left(\frac{E_c L}{V_{DD} - \Delta I R_D + R_S} \right)^2 \right]^{1/2}\tag{5.9}$$

Assuming one electron charge per reaction center, the number of reaction centers immobilized on the area $Z \times L$ can be calculated as,

$$N_{PSI} = \frac{\Delta I Z L}{q G} \left[1 + \left(\frac{E_c L}{V_{DD} - \Delta I R_D + R_S} \right)^2 \right]^{1/2}\tag{5.10}$$

Here, R_D and R_S are drain and source contact resistances, respectively and L is the source-drain spacing as shown in Figure 5.10. As PS I reaction centers have the chances to be immobilized on the non-metalized part of the AlGaN surface, integration has been done for the length measuring source to drain distance rather than for the gate length only.

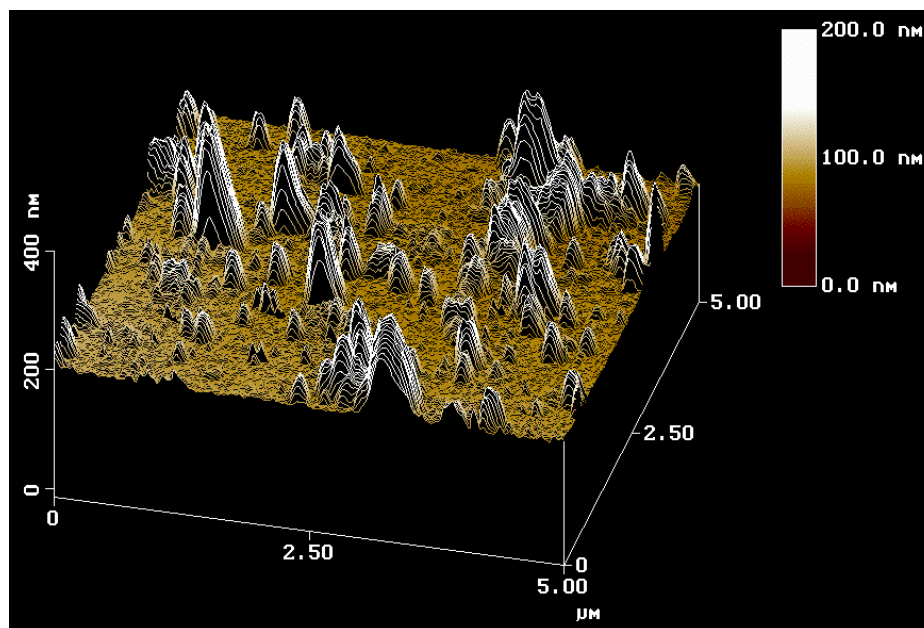


Figure 5.11: AFM image of the pure gate Au surface. The roughness of the surface can be understood from the hillocks in the AFM image and RMS roughness was measured as 24.4 nm.

5.6 Discussion

For V_{DS} of 1.00V, ΔI was measured to be 1.8 mA. Using the experimental values and the modeling constants from Table 1 in equation (10), 4.47×10^7 number of light-active reaction centers is calculated. For atomically flat surface and closed packed orientation, a maximum of 4.8×10^7 of reaction centers can sit on the gate and non-metalized surfaces. In practice, not all the molecules would be vertically oriented and continuously spaced due to surface adulation (Figure 5.11). The RMS value of the surface roughness is considered for calculation of the distance between the 2-DEG and the PS I charge centers. However, the effective charges of PS I reaction centers depend on the orientation on the surface. Hence, the calculated number of reaction centers is slightly less than the maximum number of reaction centers. V_{FG} induced by the reaction centers is

0.4 V as calculated from equation (5.4). The effective number of light-active reaction centers slightly decreases with the increase in drain-to-source voltage as shown in Figure 5.12. The number of reaction centers at 3.00V is 1.2 times less than the number at 1.00 V. The decrease in effective surface charges can be explained by the leakage current flowing between drain to gate causing void of the charges [74]. The leakage current increases with the increase in drain electric field [74] and thus decrease the effective charges on the surface with the increase in drain-to-source bias.

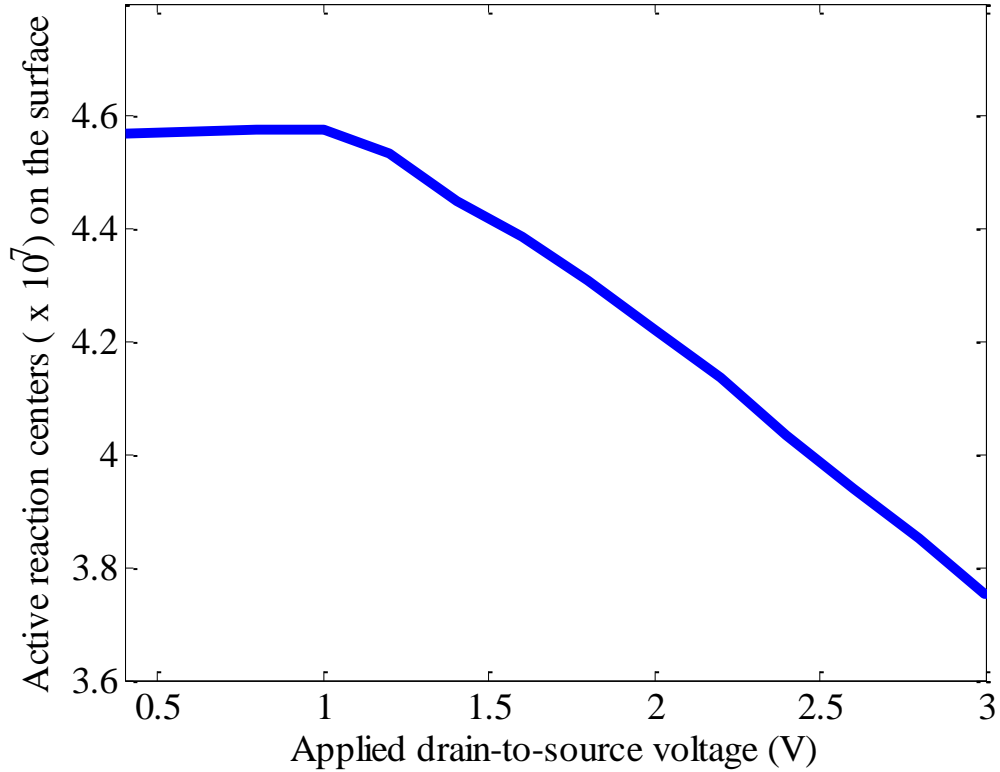


Figure 5.12: Calculated numbers of reaction centers with the applied drain-to-source voltages

Chapter 6 Conclusion and Future Work

GaN as wide bandgap material shows greater prospects for the construction of high-speed and high-power devices operating at higher temperatures compared to Si and GaAs. On the other hand, due to heterojunction, HEMT/MODFET offers the highest mobilities among the different structures of field effect devices. Combining material and device properties,, AlGaN/GaN HEMT is most promising for the integrated high-speed, high-power and high-temperature operations. Moreover, AlGaN/GaN HEMT shows great potential for sensor applications. To take advantage of such different applications of AlGaN/GaN HEMT, accurate modeling of the device is required to predict and optimize the performances before implementation of the circuit. Physics based analytical model can provide deep insight into the device behavior. A temperature dependent physics based model of AlGaN/GaN HEMT is required under different operating conditions such as dc, small and large signal ac. In this research, following contributions have been made in the field of AlGaN/GaN HEMT research:

- Development of new current-voltage expression based on nonlinear charge control method
- Development of temperature dependent analytical model for various operating conditions
- AlGaN/GaN HEMT based detection and characterization of bio-molecules
- Development of analytical model to estimate the number of bio-molecules with effective orientation on the gate surface of the AlGaN/GaN HEMT

Future Works

AlGaIn/GaN HEMT is a newer technology compared to Si or CMOS. Gate leakage, traps and surface defects are some of the barriers to the commercialization of this high performance wideband gap device. With the increase in temperature, the undesired effects become more prominent in devices. Hence, including the effects of following phenomena with temperature would help understand the device behavior more accurately:

- Parasitic parallel conduction for higher gate voltage
- Variation of drain and source resistances with gate voltage and temperature
- Leakage currents
- Trapping effects

In this work, the dc current-voltage characteristics of AlGaIn/GaN HEMT have been validated by the measured data for varying temperature. The future work can include measurement of temperature dependent small and large signal parameters as function of temperature and comparison with the measured data.

References

- [1] U. K. Mishra, P. P. Parikh, and Y. F. Wu, "AlGaIn/GaN HEMTs—An Overview of Device Operation and Applications," *Proceedings of the IEEE*, vol. 90, no.6, June 2002
- [2] E. O. Johnson, "Physical limitations on frequency and power parameters of transistors," *RCA Rev.*, pp. 163-177, 1965
- [3] B. J. Baliga, "Semiconductors for high-voltage, vertical channel FET's," *J. Appl. Phys.*, vol. 53, pp. 1759-1764, 1982.
- [4] K. Szenai, R. S. Scott, and B. J. Baliga, *IEEE Electron. Dev.* 10, 85~1989.
- [5] A. A. Lebedev and V. E. Chelnokov, "Wide-gap semiconductors for high-power electronics," *Semiconductors*, vol. 33, no. 9, pp. 999 – 1001, 1999.
- [6] D. A. Neamen, *Semiconductor Physics and Devices*, McGraw-Hill, New York, 2003.
- [7] M. Willander, M. L. Friesel, Q. Wahab, and B. Straumal, "Silicon carbide and diamond for high temperature device applications," *J. Materials Science: Materials in Electronics*, vol. 17, pp. 1-25, 2006.
- [8] P. M. Solomon, and H. Morkoc, "Modulation-doped GaAs/AlGaAs heterojunction field-effect transistors (MODFET's), ultrahigh-speed device for supercomputers," *IEEE Trans. Elec. Dev.*, vol. ED-31, no.8, Aug. 1984.
- [9] M. Morkoc, and P. M. Solomon, "The HEMT: A superfast transistor," *IEEE Spectrum*, vol. 21, pp. 28-35, Feb. 1984.
- [10] R. Dingle, H. Stormer, A. C. Gossard, and W. Wiegmann, "Electron mobilities in modulation doped semiconductor heterojunction superlattices," *Appl. Phys. Lett.*, vol. 31, pp. 665-667, 1978.
- [11] L. Esaki, and R. Tsu, "Superlattice and negative conductivity in semiconductors," *IBM Internal Res. Rep.*, RC2418, Mar. 26, 1969.
- [12] M. A. Khan, A. Bhattarai, J. N. Kuznia, and D. T. Olson, "High electron mobility transistor based on a GaN-Al_xGa_{1-x}N heterojunction," *Appl. Phys. Lett.*, vol. 63, no. 9, pp. 1214-1215, 1993.
- [13] L. F. Eastman, V. Talik, V. Kaper, J. Smart, R. Thompson, B. Green, J. R. Shealy, and T. Prunty, "Progress in High-Power, High-Frequency AlGaIn/GaN HEMTs," *phys. stat. sol.*, vol (a) 194, no. 2, pp. 433-438, 2002.
- [14] O. Ambacher, J. Smart, J. R. Shealy, N. G. Weimann, K. Chu, M. Murphy, W. J. Schaff, and L. F. Eastman, R. Dimitrov, L. Wittmer, M. Stutzmann, W. Rieger and J. Hilsenbeck, "Two-dimensional electron gases induced by spontaneous and piezoelectric polarization charges in N- and Ga-face AlGaIn/GaN heterostructures," *J. Appl. Phys.*, vol. 85, no. 6, pp. 3222-3233, 1999.
- [15] L. F. Eastman, and U. K. Mishra, "The Toughest" *IEEE Spectrum*, pp. 28-33, May 2002.
- [16] Fujitsu Laboratories Ltd., "Fujitsu Achieves Breakthrough Output with Gallium Nitride HEMT Amplifier," Kawasaki, December 8, 2003 [Online]. Available: <http://www.fujitsu.com/global/news/pr/archives/month/2003/20031208-03.html>.
- [17] NEC Corporation, "NEC Develops High-Power Gallium Nitride Transistor Amplifier for 3G Base Stations," Tokyo, August 18, 2006 [Online]. Available: <http://www.nec.co.jp/press/en/0608/1801.html>.
- [18] P. G. Neudeck, R. S. Okojie, and L. Y. Chen, "High-Temperature Electronics – A Role for Wide Bandgap Semiconductors?," *Proceedings of the IEEE*, vol. 90, no. 6, pp. 1065-1076, 2002.
- [19] J. B. Chang, "Functionalized polythiophene thin-film transistors for low-cost gas sensor arrays," A doctoral dissertation, Dept. of Electrical Engineering and Computer Sciences, Univ. of California, Berkeley, Apr. 2006.
- [20] D. Russell. Field Portable Electrochemical Sensors for Uranium and Other Sensors for Uranium and Other Species in Aqueous Samples. Department of Chemistry, Boise State University, Boise, ID, [Online]. Available: <http://www.frtr.gov/pdf/meetings/dec05/russell.pdf>
- [21] C. Bartic and G. Borghs, "Organic thin-film transistors as transducers for (bio) analytical applications," *J. of Analytical and Bioanalytical Chemistry*, vol. 384(2), pp. 354-365, Jan. 2006[5]
- [22] D. Delagebeaudeuf and N. T. Linh, "Metal-(n) AlGaAs-GaAs two-dimensional electron gas FET," *IEEE Trans. Elec. Dev.*, vol. ED-29, no.6, June 1982
- [22] H. F. Huq, Ph.D. Dissertation, The University of Tennessee, 2006

- [23] D. Delagebeaudeuf and N. T. Linh, "Metal-(n) AlGaAs-GaAs two-dimensional electron gas FET," *IEEE Trans. Elec. Dev.*, vol. ED-29, no.6, June 1982.
- [24] K. Lee, M. S. Shur, T. J. Drummond and H. Morkoc, *IEEE Trans. Electron Devices* ED-30, 207 (1983)
- [25] L. P. Sandwick, and K. L. Wang, *IEEE Trans. Electron Devices* ED-33, 651 (1986).
- [26] G. Salmer, J. Zimmermann, and R. Fauquembergue, *IEEE Trans. Microwave Theory Tech.* 36, 1124 (1988).
- [27] Rashmi, S. Haldar, and R. S. Gupta, "2-D Analytical model for current-voltage characteristics and output conductance of AlGaN/GaN MODFET," *Microwave and Optical Technology Lett.*, vol.29, no.2, pp. 117-119, 2001.
- [28] J. C. Sippel, S. S. Islam, and S. S. Mukherjee, "A physics-based analytical model of a GaN/AlGaN HEMT incorporating spontaneous and piezoelectric polarization," proceedings of IEEE, 2004.
- [29] A. F. M. Anwar, Ph.D. Dissertation, The University of Connecticut, 1988.
- [30] C. S. Chang, and H. R. Fetterman, "An analytic model for high-electron mobility transistors," *Solid State-Electron.*, vol. 30, no. 5, pp. 485 – 491, 1987
- [31] H. Morkoc, and H. Unlu, Factors affecting the performance of (Al, Ga)As/GaAs and (Al, Ga)As/InGaAs modulation-doped field-effect transistors: microwave and digital applications, Chap 2, Semiconductors and Semimetals, vol. 24, pp. 135-201, *Academic Press*, New York, 1987
- [32] A. Shey, and W. H. Ku, *IEEE Trans. Electron Devices* ED-36, 2299 (1989)
- [33] N. Dasgupta, and A. Dasgupta, "An analytical expression for sheet carrier concentration vs gate voltage for HEMT modeling," *Solid-State Electron.*, vol. 36, no. 2, pp. 201-203, 1993
- [34] L. F. Eastman. (2000, Sept.) High power, broadband, linear, solid state amplifier. Cornell Univ., Ithaca, NY. [Online]. <http://www.iiv.cornell.edu/www/schaff/muri/reports/fv01q4/report.html>
- [35] J. W. Palmour, S. T. Sheppard, R. P. Smith, S. T. Allen, W. L. Pribble, T. J. Smith, Z. Ring, J. J. Sumakeris, A. W. Saxler, and J. W. Milligan, "Wide bandgap semiconductor devices and MMIC's for RF power applications," in *Int. Electron Devices Meeting Tech. Dig.*, Washington, DC, 2001, pp. 17.4.1–17.4.4
- [36] I. P. Smorchkova, M. Wojtowicz, R. Sandhu, R. Tsai, M. Barsky, C. Namba, P.-S. Liu, R. Dia, M. Truong, D. Ko, J. Wang, H. Wang, and A. Khan, "AlGaN/GaN HEMTs—Operation in the K-Band and Above," *IEEE Transac. Microwave theory and techniques*, vol. 51, no. 2, Feb. 2003
- [37] J. S. Moon, M. Micovic, P. Janke, P. Hashimoto, W. S. Wong, R. D. Widman, L. McCray, A. Kurdoghlian, and C. Nguyen, "GaN/AlGaN HEMT's operating at 20 GHz with continuous-wave power density >6W/mm," *Electron. Lett.*, vol. 37, pp. 528–530, Apr. 2001
- [38] A. Jarndal, B. Bunz, and G. Kompa, "Accurate Large-Signal Modeling of AlGaN-GaN HEMT Including Trapping and Self-Heating Induced Dispersion," *Proceedings of the 18th International Symposium on Power Semiconductor Devices & IC's*, June 4-8, 2006 Naples, Italy.
- [39] S. Nuttinck, E. Gebara, J. Laskar, J. Shealy, and M. Harris, "Improved RF Modeling Techniques for Enhanced AlGaN/GaN HFETs," *IEEE Microwave and Wireless Component Lett.*, vol. 13, no. 4, April 2003.
- [40] Berroth, E. Chigaeva, I. Dettmann, N. Wieser, W. Vogel, H. Roll, F. Scholz, and H. Schweizer, "Advanced Large signal modeling of GaN-HEMTs," *High Performance Devices, Proceedings. IEEE Lester Eastman Conference*, 2002.
- [41] Y. Chang, Y. Zhang, Y. Zhang, and K. Y. Tong, "A thermal model for static current characteristics of AlGaN/GaN high electron mobility transistors including self-heating effect," *Journal of Appl. Physics*, vol. 99, pp.044509-1 – 044509-5, 2006
- [42] I. Ahmad, V. Kasisomayajula, M. Holtz, J. M. Berg, S. R. Kurtz, C. P. Tigges, A. A. Allerman, and A. G. Baca, "Self-heating study of an AlGaN/GaN-based heterostructure field-effect transistor using ultraviolet micro-Raman scattering," *Appl. Phys. Lett.*, vol. 86, no. 173503, pp. 1 – 3, 2006
- [43] S. C. Binari, K. Ikossi, J. A. Roussos, W. Kruppa, D. Park, H. B. Dietrich, D. D. Koleske, A. E. Wickenden, and R. L. Henry, "Trapping Effects and Microwave Power Performance in AlGaN/GaN HEMTs," *IEEE Trans. Elect. Dev.*, vol. 48, no. 3, pp. 465 – 471, 2001

- [44] C. Lu, X. Xie, X. Zhu, D. Wang, Arif Khan, I. Diagne, and S. N. Mohammad, "High-temperature electrical transport in $\text{Al}_x\text{Ga}_{1-x}\text{N}/\text{GaN}$ modulation doped field-effect transistors," *J. of Appl. Phys.*, vol. 100, no. 113729, pp. 1- 9, 2006
- [45] S. Arulkumaran, Z.H. Liu, G.I. Ng, W.C. Cheong, R. Zeng, J. Bu, H. Wang, K. Radhakrishnan, C.L. Tan, "Temperature dependent microwave performance of $\text{AlGaIn}/\text{GaIn}$ high-electron-mobility transistors on high-resistivity silicon substrate," *Thin Solid Films*, vol. 515, pp. 4517 – 4521, 2007.
- [46] J. D. Albrecht, R. P. Wang, P. P. Ruden, M. Farahmand and K. F. Brennan, "Electron transport characteristics of GaN for high temperature device modeling," *J. Applied Phys.*, vol. 83, no. 9, pp. 4777-4781, 1998.
- [47] Chang Y, Tong KY, Surya C. Numerical simulation of current–voltage characteristics of $\text{AlGaIn}/\text{GaIn}$ HEMTs at high temperatures. *Semicond Sci. Technol* 2005; 20(2): 188-92.
- [48] A. Ahmed, S. S. Islam, A. F. M. Anwar, "A Temperature-Dependent Nonlinear Analysis of $\text{GaIn}/\text{AlGaIn}$ HEMTs using Volterra Series," *IEEE Trans. Microwave Theory Tech.*, vol. 49, no. 9, pp. 1518-1524, 2001
- [49] M. A. Reed, "Molecular-Scale Electronics," *Proc. of IEEE*, vol. 87, no.4, pp. 652-658, Apr. 1999
- [50] J. Reichert, R. Ochs, D. Beckmann, H. B. Weber, M. Mayor, and H. v. Löhneysen, "Driving Current through Single Organic Molecules," *Physical Rev. Lett.*, vol. 88, no. 17, pp. 176804-1 - 176804-4, Apr. 2002
- [51] D. B. Janes, S. Ghosh, J. Choi, S. Lodha, and S. Bhattacharya, "Circuit Characteristics of Molecular Electronic Components," *Proc. of IEEE International conf. on Application-Specific Systems, Architectures, and Processors*, pp. 121-131, June 2003
- [52] B. A. Mantooth and P. S. Weiss, "Fabrication, Assembly, and Characterization of Molecular Electronic Components," *Proc. of the IEEE*, vol. 91, no.11, pp.1785-1802, Nov. 2003
- [53] J. M. Tour, A. M. Rawlett, M. Kozaki, Y. Yao, R. C. Jagessar, S. M. Dirk, D. W. Price, M. A. Reed, C. Zhou, J. Chen, W. Wang, and I. Campbell, "Synthesis and Preliminary Testing of Molecular Wires and Devices," *Chem. Eur. J.*, vol.7, no. 23, pp. 5118-5134, Nov. 2001
- [54] Sze SM. *Physics of semiconductor devices*. Wiley, New York, 1981, 2nd ed
- [55] X. H. Wu, L. M. Brown, D. Kapolnek, S. Keller, B. Keller, S. P. Den-Baars, and J. S. Speck, *J. Appl. Phys.* 80, 3228, 1996
- [56] C. Wei, Y. A. Tkachenko, and Dylan Bartle, "An Accurate Large-Signal Model of GaAs MESFET which accounts for Charge Conservation, Dispersion, and Self-Heating," *IEEE Trans. Microwave Theory and Techniques*, vol. 46, no. 11, pp. 1638-1644, 1998
- [57] H.F. Cooke, "Precise technique finds FET thermal Resistance," *Microwaves & RF*, pp. 85-87, 1986
- [58] Jon C. Freeman, "Channel Temperature Model for Microwave $\text{AlGaIn}/\text{GaIn}$ Power HEMTs on SiC and Sapphire," *IEEE MTT-S Digest*, pp. 2031-2034, 2004
- [59] J. Zou, D. Kotchetkov, A. A. Balandin, D. I. Florescu, and F. H. Pollak, "Thermal conductivity of GaN films: Effects of impurities and dislocations," *J. Appl. Phys. Lett.*, vol. 92, no. 51, pp. 2534-2539, 2002
- [60] A. M. Darwish, A. J. Bayba, and H. A. Hung, "Accurate Determination of Thermal Resistance of FETs," *IEEE Trans. Microwave theory and Technique*, vol. 53, no. 1, pp. 306-313, 2005
- [61] Y. S. Chauhan, C. Anghel, F. Krummenacher, C. Maier, Renaud Gillon, Benoit Bakeroot, Bart Desoete, S. Frere, A. B. Desormeaux, A. Sharma, M. Declercq, A. M. Ionescu, "Scalable general high voltage MOSFET model including quasi-saturation and self-heating effects," *Solid-State Electronics*, vol. 50, pp. 1801–1813, 2006.
- [62] Yu ET, Sullivan GJ, Asbeck PM, Wang CD, Qiao D, Lau SS. Measurement of piezoelectrically induced charge in $\text{GaIn}/\text{AlGaIn}$ heterostructure field-effect transistor. *Appl Phys Lett* 1997; 71: 2794-96
- [63] Varshni YP. Temperature dependence of the energy gap in semiconductors. *Physica* 1967; 34(1): 149
- [64] Guo O, Yoshida A. Temperature dependence of band gap change in InN and AlN . *Jpn. J Appl Phys* 1994; 33: 2453-56
- [65] Vurgaftman I, Meyer JR, Ram-Mohan LR. Band parameters for III-V compound semiconductors and their alloys. *J. Appl Phys* 2001; 89: 5815-75

- [66] M. A. Huque and T. Rahman, Group work
- [67] Ramvall P, Aoyagi Y, Kuramata A, Hacke P, Horino K. Influence of a piezoelectric field on the electron distribution in a double GaN/Al_{0.14}Ga_{0.86}N heterojunction. *Appl Phys Lett* 1999; 74: 3866-68
- [68] Rashmi, Halder S, Gupta RS. 2-D analytical model for current-voltage characteristics and output conductance of AlGaIn/GaN MODFET. *Microwave and Optical Tech Lett* 2001; 29(2): 117-23
- [69] Ambacher O, Majewski J, Miskys C, Link A, Hermann M, Eickhoff M, et al. Pyroelectric properties of Al(In)GaIn/GaN hetero- and quantum well structures. *J Phys: Condens Matter* 2002; 14: 3399-34
- [70] Shur MS, Bykhovshki AD, Gaska R. Pyroelectric and Piezoelectric Properties of GaN-Based Materials. *MRS Internet J Nitride Semicond Res* 1999; 4S1, G1.6
- [71] Mnatsakanov TT, Levinshtein ME, Pomortseva LI, Yurkov SN, Simin GS, Khan MA. Carrier mobility model for GaN. *Solid-State Electron* 2003; 47: 111-15
- [72] Li M and Wang Y. 2-D analytical model for current-voltage characteristics and transconductance of AlGaIn/GaN MODFETs. *IEEE Trans Electron Dev* 2008; 55(1): 261-7.
- [73] X. Z. Dang, P. M. Asbeck, E. T. Yu, G. J. Sullivan, M. Y. Chen, and B. T. McDermott, K. S. Boutros and J. M. Redwing, "Measurement of drift mobility in AlGaIn/GaN heterostructure field-effect transistor" *Applied Physics Letters*, vol.74, no.25, pp. 3890 – 3892, June, 1999
- [74] W. Saito, M. Kuraguchi, Y. Takada, K. Tsuda, I. Omura, T. Ogura, "Influence of surface defect charge at AlGaIn–GaN–HEMT upon Schottky gate leakage current and breakdown voltage," *IEEE Trans. Elec. Dev.*, 2005.
- [75] P. Revva, J. M. Langer, M. Missous, and A. R. Peaker, "Temperature dependence of the Schottky barrier in Al/AlGaAs metal-semiconductor Junctions, " *J. Appl. Phys.* 74 (1), 1 pp. 416-425, July 1993
- [76] Stutzmann M, Steinhoff G, Eickhoff M, Ambacher O, Nebel CE, Schalwig J, Neuberger R, Müller G. GaN-based heterostructures for sensor applications. *Diamond Rel Mater* 2002; 11:886-91
- [77] Neuberger R, Muller G, Ambacher O, Stutzmann M. High-Electron-Mobility AlGaIn/GaN Transistors (HEMTs) for Fluid Monitoring Applications. *Phys Status Solidi A* 2001; 185(1):85-9
- [78] Schalwig J, Muller G, Ambacher O, Stutzmann M. Group-III-Nitride Based Gas Sensing Devices. *Phys Status Solidi A* 2001; 185(1):39-45
- [79] Steinhoff G, Hermann M, Schaff WJ, Eastman LF, Stutzmann M, Eickhoff M. pH response of GaN surfaces and its application for pH-sensitive field-effect transistors. *Appl Phys Lett* 2003; 83(1):177-9
- [80] Eickhoff M, Neuberger R, Steinhoff G, Ambacher O, Muller G, Stutzmann M. Wetting behaviour of GaN surfaces with Ga- or N-face polarity. *Phys Status Solidi B* 2001; 228(2):519-22
- [81] Schalwig J, Muller G, Eickhoff M, Ambacher O, Stutzmann M. Gas sensitive GaN/AlGaIn-heterostructures. *Sens Actuat B* 2002; 87: 425-30
- [82] I. Lee, J. W. Lee, and E. Greenbaum, "Biomolecular Electronics: Vectorial Arrays of Photosynthetic Reaction Centers," *Physical Rev. Lett.*, vol. 79, no. 17, pp. 3294 – 3297, 1997.
- [83] P. R. Chitnis, "Photosystem I," *Plant Physiol.*, vol. 111, pp. 661-669, 1996.
- [84] I. Lee, J.W. Lee, A. Stubna, and E. Greenbaum, "Measurement of Electrostatic Potentials above Oriented Single Photosynthetic Reaction Centers," *J. Phys. Chem. B*, vol. 104, no. 11, pp. 2439-2443, Jan. 2000

Vita

Sazia Afreen Eliza received her B. Sc. and M. Sc. from the department of Electrical and Electronic Engineering (EEE) at Bangladesh University of Engineering and Technology (BUET), Dhaka, Bangladesh in 2003 and 2005, respectively. From 2003 to 2005, she worked as a lecturer in the department of EEE at BUET. She has been pursuing her Ph. D. program in the department of Electrical Engineering and Computer Science at the University of Tennessee, Knoxville, USA since August 2005. Her doctoral research is focused on the modeling of GaN based devices for the applications of high-power, high-frequency, high-temperature circuits and sensors. She has publications in journals and conference proceedings. Her fields of interests are wide bandgap semiconductor based devices, analog and digital circuit design, nanotechnology and bio-sensors.